POLITECNICO DI TORINO
Repository ISTITUZIONALE

Cross-code comparison of the edge codes SOLPS-ITER, SOLEDGE2D and UEDGE in modelling a high-power neon-seeded scenario in the DTT

Original
Cross-code comparison of the edge codes SOLPS-ITER, SOLEDGE2D and UEDGE in modelling a high-power neon-seeded scenario in the DTT / Moscheni, M., Wigram, M., Wu, H., Meineri, C., Carati, C., De Marchi, E., Greenwald, M., Innocente, P., Labombard, B., Subba, F., Zanino, R.. - In: NUCLEAR FUSION. - ISSN 0029-5515. - 65:2(2025), pp. 1-26. [10.1088/1741-4326/ada048]

Availability:
This version is available at: 11583/3002920 since: 2025-09-10T16:03:06Z

Publisher:
Institute of Physics

Published
DOI:10.1088/1741-4326/ada048

Terms of use:

This article is made available under terms and conditions as specified in the corresponding bibliographic description in the repository

Publisher copyright

(Article begins on next page)

19 November 2026

nuclear fusion
IAEA

PAPER • OPEN ACCESS

Cross-code comparison of the edge codes SOLPS-ITER, SOLEDGE2D and UEDGE in modelling a high-power neon-seeded scenario in the DTT

To cite this article: M. Moscheni *et al* 2025 *Nucl. Fusion* **65** 026025

View the article online for updates and enhancements.

You may also like

- Interpretative transport modeling of the WEST boundary plasma: main plasma and light impurities
A. Gallo, A. Sepetys, Y. Marandet et al.
- Self-consistent cross-field transport model for core and edge plasma transport
S. Baschetti, H. Bufferand, G. Ciraolo et al.
- 3D numerical study of neutral gas dynamics in the DTT particle exhaust using the DSMC method
C. Tantos, S. Varoutis, V. Hauer et al.

This content was downloaded from IP address 130.192.181.37 on 10/09/2025 at 16:56

OPEN ACCESS
IOP Publishing | International Atomic Energy Agency
Nuclear Fusion
Nucl. Fusion **65** (2025) 026025 (26pp)
https://doi.org/10.1088/1741-4326/ada048

Cross-code comparison of the edge codes SOLPS-ITER, SOLEDGE2D and UEDGE in modelling a high-power neon-seeded scenario in the DTT

M. Moscheni[1,2,*], M. Wigram[3], H. Wu[1], C. Meineri[1], C. Carati[4], E. De Marchi[4], M. Greenwald[3], P. Innocente[5], B. LaBombard[3], F. Subba[1] and R. Zanino[1]

[1] NEMO Group, Dipartimento Energia, Politecnico di Torino, Corso Duca degli Abruzzi 24, 10129 Torino, Italy
[2] Tokamak Energy Ltd, 173 Brook Drive, Milton Park, Abingdon, United Kingdom of Great Britain and Northern Ireland
[3] MIT Plasma Science and Fusion Center, Cambridge, MA 02139, United States of America
[4] Eni S.p.A., Roma 00144, Italy
[5] Consorzio RFX, corso Stati Uniti, 4, Padova, Italy

E-mail: mosca_matteo@hotmail.com

Received 12 July 2024, revised 15 October 2024
Accepted for publication 17 December 2024
Published 6 January 2025

Abstract

In this work, we cross-compare the state-of-the-art edge plasma codes SOLPS-ITER, SOLEDGE2D, and UEDGE in a reactor-relevant neon-seeded Divertor Tokamak Test scenario at nominal power, extending the simplified test-bed of Moscheni *et al* (2022 *Nucl. Fusion* **62** 056009). Converged solutions targeting the same separatrix density and radiated power are obtained by adjusting the pumping albedo and the neon puffing rate. This higher-power scenario is generally characterised by substantial disagreement between the three codes, up to 78%–178% in peak heat fluxes. Discrepancies found in Moscheni *et al* (2022 *Nucl. Fusion* **62** 056009) are indeed exacerbated, and new ones arise. Underlying causes include the over-penetration of neutrals implied by the unified ion-neutral temperature of UEDGE (observed in Moscheni *et al* (2022 *Nucl. Fusion* **62** 056009)), here resulting in a 38%–114% over-estimation of core plasma densities. The particular set of EIRENE atomic-molecular reactions adopted is found to stiffly restrict the achievable code solutions, which results in the predicted effective charge Z_{eff} changing from ∼5 to ∼8 at the outer mid-plane separatrix. The strong link between Z_{eff}, main ion density and unified ion temperature emphasises the need of proper assessments of impurity cross-field transport, with its implications on core contamination and wall erosion. The advantages of extended plasma meshes are found to come with associated modelling intricacies, yet to be fully characterised but seemingly impacting on the activity around the secondary X-point of single-null magnetic topologies. An appreciable impurity particle imbalance, generated by the neon ion density floor, is noted—speculatively contributing

* Author to whom any correspondence should be addressed.

Original Content from this work may be used under the terms of the Creative Commons Attribution 4.0 licence. Any further distribution of this work must maintain attribution to the author(s) and the title of the work, journal citation and DOI.

to SOLEDGE2D's different radiation emission distribution, and expected to be even more deleterious for high-Z impurities in all the codes. Potential drivers of further discrepancies are the different Braginskii formulations of collision times and momentum sources in presence of impurities, and the SOLPS-ITER extra terms gaining importance around the detachment front. Outstanding questions unanswered in this work prompt further investigations.

Keywords: DTT, scrape-off layer, power exhaust, edge modelling, SOLPS-ITER, SOLEDGE2D, UEDGE

(Some figures may appear in colour only in the online journal)

1. Introduction

One of the outstanding open issues remaining to be resolved for the realisation of tokamak-based fusion energy is the power exhaust. The combination of high core plasma energy content for power generation, high edge confinement leading to narrow scrape-off layer heat flux widths [1, 2], and the variety of plasma-wall interactions occurring at the interface with the plasma-facing components (PFCs), makes the power exhaust a complex problem.

The ITER exhaust strategy foresees, on the edge-plasma side, a conventional single-null magnetic topology, with extrinsic impurities seeded to ameliorate the otherwise-prohibitive plasma heat fluxes on the divertor target plates [3]. From the PFC perspective instead, the ITER divertor relies upon water-cooled tungsten-monoblock technology, with a capability of exhausting steady-state heat loads in excess of $\sim 10\,\mathrm{MW}\cdot\mathrm{m}^{-2}$ successfully verified [4].

Nonetheless, whilst such an approach may suffice for ITER, this is not guaranteed to meet the demands of nuclear fusion pilot plants like EU-DEMO [5] or ARC [6], due to the substantially higher power densities and consequent heat fluxes in such devices, and more stringent PFC lifetime requirements. Power exhaust studies are thus increasingly focused on advanced magnetic configurations [7–9] and liquid-metal PFCs [10, 11], both potential alternative solutions being experimentally tested. However, such testing still falls short of conclusively demonstrating reactor relevancy to date.

The Divertor Tokamak Test (DTT) is currently being built in Italy and, with its input power $P_{\mathrm{in}} = 45\,\mathrm{MW}$, plasma current $I_{\mathrm{p}} = 5.5\,\mathrm{MA}$, and magnetic field on axis $B_0 = 6\,\mathrm{T}$, presents a reactor-relevant power exhaust experimental device. Flexibility to accommodate numerous advanced magnetic equilibria is included in the design, and later major upgrades in the life of the machine will feature liquid-metal PFCs [12].

Designing this machine heavily relied upon two-dimensional edge plasma modelling with fluid codes [13, 14], indeed one of the primary workhorses of the divertor design phase and edge plasma experimental data interpretation in any tokamak. Three such state-of-the-art modelling suites that are utilised in this study are SOLPS-ITER [15], SOLEDGE2D [16], and UEDGE [17]. Though fundamentally very similar—relying upon 2D Braginskii plasma equations, diffusive cross-field anomalous transport, neutral/impurity physics, etc—the exact implementation of the models differs between the codes. The impact these differences and model choices impose is unclear and yet important to understand and interpret the simulation predictions from any of the code suites.

These three edge codes were previously cross-compared in a pure-deuterium low-power DTT environment [18], to assess the code predictions in modelling the same scenarios in reactor-relevant conditions of heat flux and power decay length (λ_q). Building on the study and lessons learnt in [18], focus of the present work is extending the investigations to a high-power, neon-seeded DTT scenario, running each code with their most usually adopted settings in this context. The level of discrepancy of predictions and underlying explanations are then evaluated.

Although these DTT-centred predictive works are essential for providing insights into the model/geometry errors of the codes, their accuracy cannot be quantified. This will therefore be part of a separate publication focused on a comparison against Alcator C-Mod experimental data [19].

The paper is organised as follows. Section 2 dissects the features of the different equations solved by the simulation tools, highlighting the differences with respect to [18]. In section 3, the meshes, input settings, and boundary conditions of the simulation setups are presented. Section 4 compares the outcomes of the simulations, commenting upon regions of both agreement and disagreement. Underlying reasons behind the discrepancies observed are then scrutinised and expounded in section 5. Finally, section 6 outlines the conclusions inferred by the present work.

2. Simulation codes: SOLPS-ITER, SOLEDGE2D, UEDGE

Throughout the sections below, labels a and b generally denote charged species, z and w the neon ionisation stages in particular. The species existing in the simulations are grouped as follows: $\mathcal{S}^+ = \{\mathrm{D}^+\} \cup \{\mathrm{Ne}^{z+}\}_{z=1}^{z=10}$; $\mathcal{S}^{\pm} = \mathcal{S}^+ \cup \{\mathrm{e}\}$; $\mathcal{S}^0 = \{\mathrm{D}\,;\,\mathrm{D}_2\,;\,\mathrm{D}_2^+\,;\,\mathrm{Ne}\}$ for SOLPS-ITER and SOLEDGE2D, $\mathcal{S}^0 = \{\mathrm{D}\,;\,\mathrm{Ne}\}$ in UEDGE; $\mathcal{S}^{0+} = \mathcal{S}^0 \cup \mathcal{S}^+$.

2.1. Plasma and impurity models

The complete set of equations solved by each code can be found at [15] for SOLPS-ITER (version 3.0.7), [16] for

SOLEDGE2D (latest version), and [20] for UEDGE (version 7.06).

In the following subsections, the equations presented neglect drifts and electric currents, omit the geometric factors arising from differentiating in a toroidal geometry, and only aim at highlighting the differences arising between the set of equations provided in [18] (with no impurity species) and the models employed in this work (with impurity species active). As such, quantities that are not commented upon in this section are assumed to match their counterparts in [18].

2.1.1. Ion continuity equations. With the presence of ten neon ionisation stages in addition to D^+ in $\mathcal{S}^+$, the three codes separately solve the coupled particle transport of the $N_{\mathcal{S}^+} = 11$ species, whose mathematical form matches equation (1) of [18] (hence not leveraging the so called 'fixed-fraction' simplified model [21]).

Atomic rates of electron ionisation (EI) and recombination (RC) are computed from the ADAS database [22] in SOLPS-ITER and SOLEDGE2D, from STRAHL [23, 24] in UEDGE—with the consequences being detailed in section 5.3.5.1. All the three codes neglect particle sources due to charge exchange (CX) reactions within $\{\mathrm{Ne}^{z+}\}_{z=1}^{z=10}$.

For radial particle transport, the same cross-field anomalous particle diffusivity is applied to all species, $D_a^{\mathrm{AN}} = D^{\mathrm{AN}}\ \forall a$.

2.1.2. Electron continuity equation. Upon computation of ion densities (section 2.1.1), the electron density follows from the quasi-neutrality condition: $n_\mathrm{e} = \sum_{a\in\mathcal{S}^+} Z_a n_a$.

2.1.3. Ion momentum equations. In the present work, all the codes leverage on the trace-impurity approximation (TIA, section 5.1.2) [25–27]. Its regime of applicability requires:

$$\text{TIA: } \frac{n_z Z_z^2}{n_{\mathrm{D}^+}} \ll 1\ \forall z \Leftrightarrow Z_0 = \sum_z \frac{n_z Z_z^2}{n_{\mathrm{D}^+}} \ll 1 \tag{1}$$

to hold or, equivalently, the impurity/impurity collision frequency to be negligible if compared to other collision frequencies (section 6.6.4 of [27]). This allows the Braginskii closure to be adopted (sections 2.1.5 and 5.1.2).

In SOLPS-ITER and SOLEDGE2D, equations (2) and (3) of [18] are generalised for impurities by adopting the subscript $a \in \mathcal{S}^+$ in place of i, with momentum viscosity $\eta_a^{\mathrm{AN}} = m_a n_a \nu^{\mathrm{AN}}$. Notable exceptions to this are: (i) the SOLPS-ITER geometrical term $\partial_x\left[\eta_{ax}^{\mathrm{CL}}\partial_x(h_z\sqrt{B})/\sqrt{B}\right]\sqrt{B}V_{a\|}$, non-zero only for D^+; (ii) the pressure-gradient force for species a which, from $\partial_x(n_\mathrm{i}T_\mathrm{i} + n_\mathrm{e}T_\mathrm{e})$ in [18], generalises to $\partial_x(n_aT_\mathrm{i}) + Z_a n_a \partial_x(n_\mathrm{e}T_\mathrm{e})/n_\mathrm{e}$. It is worthwhile noting the absence of viscosity-related terms $\eta_{ax}^{\mathrm{CL}}\partial_x V_{a\|}$ in SOLEDGE2D formulation of the momentum equations.

The SOLPS-ITER (SI) friction force $S_{ba,\mathrm{fr}}^{\mathrm{m}}$ $(= -S_{ab,\mathrm{fr}}^{\mathrm{m}})$ [28] exerted from the charged species $b \in \mathcal{S}^\pm$ on the ion species $a \in \mathcal{S}^+$ enters the equations through the momentum source $S_{a,\mathrm{fr}}^{\mathrm{m}} = \sum_{b\in\mathcal{S}^\pm} S_{ba,\mathrm{fr}}^{\mathrm{m}}$. This momentum source and the cumulative thermal force $S_{a,\mathrm{th}}^{\mathrm{m}}$ experienced by ion species a respectively read:

$$\begin{aligned} S_{a,\mathrm{fr}}^{\mathrm{m,SI}} &= \sum_{b\in\mathcal{S}^\pm} \frac{m_\gamma}{f_{\sigma_\gamma}\zeta_{\gamma b}} \sqrt{\frac{\frac{m_a}{m_\gamma}\frac{m_b}{m_\gamma}}{\frac{m_a}{m_\gamma}+\frac{m_b}{m_\gamma}}} Z_a^2 Z_b^2 n_a n_b \left(V_{b\|} - V_{a\|}\right) \\ &= \sum_{b\in\mathcal{S}^\pm} \frac{\mu_{ab}}{\sqrt{2}\tau_{ab}^{\mathrm{SI}} f_{\sigma_\gamma}} n_a \left(V_{b\|} - V_{a\|}\right) \\ S_{a,\mathrm{th}}^{\mathrm{m,SI}} &= \frac{n_a}{n_\mathrm{e}}\left(1 - \frac{Z_a}{Z_{\mathrm{eff}}}\right)\left[\frac{\partial p_\mathrm{e}}{\partial x} - e n_\mathrm{e}\frac{\partial \phi}{\partial x} - 2.65 n_\mathrm{e}\frac{\partial T_\mathrm{i}}{\partial x}\right] \end{aligned} \tag{2}$$

with $\gamma \in \{\mathrm{p} = \mathrm{D}^+; \mathrm{e} = \text{electron}\}$, $\mu_{ab} = m_a m_b/(m_a + m_b)$ being the reduced mass, $Z_\mathrm{e} = 1$ and $m_a + m_\mathrm{e} \sim m_a$ for electrons, $Z_{\mathrm{eff}} = \sum_{a\in\mathcal{S}^+} n_a Z_a^2/n_\mathrm{e}$, ϕ representing the electric potential, $f_{\sigma_\mathrm{p}} = 1$ and $f_{\sigma_\mathrm{e}} = 4.95 Z_{\mathrm{eff}}/(1 + 1.54 Z_{\mathrm{eff}})$, and:

$$\begin{aligned} \zeta_\mathrm{p} &= \frac{3}{4\sqrt{2\pi}}\left(\frac{4\pi\varepsilon_0}{e^2}\right)^2 \frac{\sqrt{m_\mathrm{p}}\,T_\mathrm{i}^{3/2}}{\ln\Lambda} \\ \zeta_\mathrm{e} &= \frac{3}{4\sqrt{2\pi}}\left(\frac{4\pi\varepsilon_0}{e^2}\right)^2 \frac{\sqrt{m_\mathrm{e}}\,T_\mathrm{e}^{3/2}}{\ln\Lambda} \\ \tau_{ab}^{\mathrm{SI}} &= \frac{\sqrt{\mu_{ab}}}{\sqrt{2m_\mathrm{p}}}\frac{1}{n_b Z_a^2 Z_b^2}\cdot\zeta_\mathrm{p} \\ \tau_{eb}^{\mathrm{SI}} &= \frac{1}{n_b Z_b^2}\cdot\zeta_\mathrm{e} \end{aligned} \tag{3}$$

with units $[\zeta_*] = \mathrm{s}\cdot\mathrm{m}^{-3}$ and $[\tau_*] = \mathrm{s}$, following the convention of [28].

In SOLEDGE2D (SE), which employs a single unified ion temperature (section 2.1.5), instead these terms read as:

$$\begin{aligned} S_{a,\mathrm{fr}}^{\mathrm{m,SE}} &= \sum_{b\in\mathcal{S}^\pm} 0.51\cdot\frac{1}{2\tau_{ab}^{\mathrm{SE}}}\left(\frac{m_a}{m_b}+\frac{m_b}{m_a}\right)\frac{n_a n_b}{\frac{n_a}{m_a}+\frac{n_b}{m_b}}\left(V_{b\|} - V_{a\|}\right) \\ S_{a,\mathrm{th}}^{\mathrm{m,SE}} &= \sum_{b\in\mathcal{S}^\pm} 0.71\cdot\frac{n_a n_b}{\frac{n_a}{m_a}+\frac{n_b}{m_b}}\left(\frac{Z_a^2}{m_a} - \frac{Z_b^2}{m_b}\right)\frac{\partial T_\mathrm{i}}{\partial x} \end{aligned} \tag{4}$$

with:

$$\tau_{ab}^{\mathrm{SE}} = \frac{n_a + n_b}{n_a n_b}\frac{3\sqrt{2}\pi^{3/2}\varepsilon_0^2 m_a m_b}{e^4 Z_a^2 Z_b^2 \ln\Lambda}\left(\frac{T_a}{m_a}+\frac{T_b}{m_b}\right)^{3/2}. \tag{5}$$

According to the TIA, the coefficients 0.51 and 0.71 $(= \sqrt{2}/2)$ in SOLEDGE2D are characteristic of the pure plasma limit $(n_z = 0\ \forall z \Leftrightarrow Z_{\mathrm{eff}} = 1)$ in the Braginskii formulation [28], and the presence of impurities is included via Z_a and Z_b in equation (5).

UEDGE solves equation (3) of [18] for $V_{\mathrm{D}^+\|}$ in the purely-diffusive approximation. Instead, a simplified momentum equation to compute the fluid velocity of the neon impurity ions is adopted, by leveraging a 'force balance' flavour of TIA which ignores both impurity inertia and viscosity [29]. The impurity parallel velocity in UEDGE is thus given by:

$$V_{z\|} = V_{\mathrm{D}^+\|}\frac{\tau_{\mathrm{eff}}}{m_\mathrm{p}}\cdot\left(-\frac{1}{n_z}\frac{\partial p_z}{\partial x} + \alpha_z\frac{\partial T_\mathrm{e}}{\partial x} + \beta_z\frac{\partial T_\mathrm{i}}{\partial x} + b_x Z_z e E_x\right) \tag{6}$$

with:

$$\tau_{\text{eff}} = \tau_{\text{pz}}^{\text{UE}} \cdot \mathcal{F}_{\lambda}^{\text{lim}} \frac{n_z}{n_{\text{e}}} \cdot \frac{(1+2.65Z_0)(1+0.285Z_0)}{(1+0.24Z_0)(1+0.93Z_0)}$$
$$\tau_{\text{pz}}^{\text{UE}} = \frac{3}{4\sqrt{2\pi}} \left(\frac{4\pi\varepsilon_0}{e^2}\right)^2 \frac{\sqrt{m_{\text{p}}}\, m_z}{Z_z^2 (m_{\text{p}} + m_z)} \frac{T_{\text{i}}^{3/2}}{n_z \ln\Lambda}$$
$$\alpha_z = \frac{2.2 \cdot Z_z^2 (1+0.52Z_{\text{eff}})}{Z_{\text{eff}} (1+2.65Z_{\text{eff}})(1+0.29Z_{\text{eff}})}$$
$$\beta_z = \frac{1.56 \cdot Z_z^2 \left(1+\sqrt{2}Z_0\right)(1+0.52Z_0)}{(1+2.65Z_0)(1+0.29Z_0)} \cdot \left[Z_0 + \sqrt{\frac{1}{2}\left(1+\frac{m_{\text{p}}}{m_z}\right)}\right]^{-1} + 0.6 \cdot \left(\frac{Z_z^2 \sum_w n_w}{\sum_w Z_w^2 n_w} - 1\right) \tag{7}$$

and $\mathcal{F}_{\lambda}^{\text{lim}}$ being a suitable flux limiter, with Z_0 defined by equation (1).

More on TIA, collision times and momentum equations is left to be commented upon in sections 5.1 and 5.2.

2.1.4. Electron momentum equation. With electric currents discarded, and velocities known from the ion momentum equations (section 2.1.3), the parallel ($\|$) and poloidal (x) macroscopic velocity of the electron fluid are retrieved from ambipolarity: $V_{\text{e}\|} = \sum_{a\in\mathcal{S}^+} Z_a V_{a\|} n_a / n_{\text{e}}$ and $V_{\text{e}x} = b_x V_{\text{e}\|}$ with $b_x = B_x/||\mathbf{B}||$.

2.1.5. Ion energy equation. All three codes do not solve for $N_{\mathcal{S}^+}$ separate ion-species-specific energy equations $\mathcal{E}[p_a]\ \forall a \in \mathcal{S}^+$, where $p_a = n_a T_a$. Instead, a unified equation for all ion species is solved for, invoking a unified ion temperature T_{i} such that $\mathcal{E}[p_{\text{i}}] = \sum_{a\in\mathcal{S}^+} \mathcal{E}[p_a]$ where $p_{\text{i}} = \sum_{a\in\mathcal{S}^+} n_a T_a = T_{\text{i}} \sum_{a\in\mathcal{S}^+} n_a = n_{\text{i}} T_{\text{i}}$. This thereby: (i) leverages on the additivity of the partial pressures p_a and linearity of the corresponding equations; and (ii) assumes an instantaneous intra-ion-species thermal equilibration leading to $T_a = T_{\text{i}}\ \forall a \in \mathcal{S}^+$.

A noteworthy feature exclusive to SOLEDGE2D is its capability of fully accounting for various ion temperatures by separately solving $\mathcal{E}[p_a]\ \forall a \in \mathcal{S}^+$. Though not analysed in the present work, the comparative assessment would be valuable—the efficiency of thermal equilibration dropping for particles of un-like mass (section 5.1.1).

By virtue of the summation $\mathcal{E}[p_{\text{i}}] = \sum_{a\in\mathcal{S}^+} \mathcal{E}[p_a]$, summation of species-specific transport coefficients results in:

$$\kappa_{\text{i}x}^{\text{CL}} = \mathcal{F}_{\text{i}}^{\text{lim}} \tilde{\kappa}_{\text{i}x}^{\text{CL}} = \mathcal{F}_{\text{i}}^{\text{lim}} \frac{5}{2} T_{\text{i}} \sum_{a\in\mathcal{S}^+} \frac{n_a \tau_a}{m_a} f_a^{\text{B}}$$
$$\kappa_{\text{i}}^{\text{AN}} = \sum_{a\in\mathcal{S}^+} \chi_a^{\text{AN}} n_a = \chi_{\text{i}}^{\text{AN}} n_{\text{i}} \tag{8}$$

with $\mathcal{F}_{\text{i}}^{\text{lim}}$ flux-limiting[6] $\tilde{\kappa}_{\text{i}x}^{\text{CL}}$, the classical (i.e. Spitzer-Härm) transport coefficient according to Braginskii formulation (implied by the factor f_a^{B}) [30], and $\chi_a^{\text{AN}} = \chi_{\text{i}}^{\text{AN}}\ \forall a \in \mathcal{S}^+$ for its anomalous counterpart.

The unified ion energy equation $\mathcal{E}[p_{\text{i}}]$ for the three codes is thus retrieved by summing expressions in the fashion of equations (4)–(6) of [18]. For SOLPS-ITER:

$$\frac{\partial}{\partial t}\left(\frac{3}{2} n_{\text{i}} T_{\text{i}}\right) + \frac{\partial}{\partial x}\left\{\frac{3}{2} T_{\text{i}} \sum_{a\in\mathcal{S}^+}\left[n_a\left(b_x V_{a\|} + \frac{5}{3} V_{ax,n}^{\text{diff}} + V_{ax}^{\text{corr}}\right)\right] - \left(\kappa_{\text{i}x}^{\text{CL}} + \kappa_{\text{i}}^{\text{AN}}\right)\frac{\partial T_{\text{i}}}{\partial x}\right\} + \frac{\partial}{\partial y}\left[\frac{5}{2} T_{\text{i}} \sum_{a\in\mathcal{S}^+}\left(n_a V_{ay,n}^{\text{diff}}\right) - \kappa_{\text{i}}^{\text{AN}} \frac{\partial T_{\text{i}}}{\partial y}\right]$$
$$= \sum_{a\in\mathcal{S}^+}\left\{-n_a T_{\text{i}} \frac{\partial\left(b_x V_{a\|}\right)}{\partial x} + \left[\left(\eta_{ax}^{\text{CL}} + \eta_a^{\text{AN}}\right)\left(\frac{\partial V_{a\|}}{\partial x}\right)^2 + \eta_a^{\text{AN}}\left(\frac{\partial V_{a\|}}{\partial y}\right)^2\right]\right\} + S_{\text{i}}^{\text{E}} \tag{9}$$

For SOLEDGE2D:

$$\frac{\partial}{\partial t}\left[\frac{3}{2} n_{\text{i}} T_{\text{i}} + \sum_{a\in\mathcal{S}^+}\left(\frac{1}{2} m_a n_a V_{a\|}^2\right)\right] + \frac{\partial}{\partial x}\left\{\sum_{a\in\mathcal{S}^+}\left[\left(\frac{5}{2} n_a T_{\text{i}} + \frac{1}{2} m_a n_a V_{a\|}^2\right) b_x V_{a\|}\right] - \kappa_{\text{i}x}^{\text{CL}} \frac{\partial T_{\text{i}}}{\partial x}\right\} + \frac{\partial}{\partial y}\left\{\sum_{a\in\mathcal{S}^+}\left[\left(\frac{5}{2} n_a T_{\text{i}} + \frac{1}{2} m_a n_a V_{a\|}^2\right) V_{ay,n}^{\text{diff}}\right] - \kappa_{\text{i}}^{\text{AN}} \frac{\partial T_{\text{i}}}{\partial y}\right\}$$
$$= \sum_{a\in\mathcal{S}^+}\left\{-b_x V_{a\|} \frac{\partial\left(n_{\text{e}} T_{\text{e}}\right)}{\partial x} + \frac{\partial}{\partial x}\left[\frac{1}{2}\eta_{ax}^{\text{CL}}\left(\frac{\partial V_{a\|}^2}{\partial x}\right)\right] + \frac{\partial}{\partial y}\left[\frac{1}{2}\eta_a^{\text{AN}}\left(\frac{\partial V_{a\|}^2}{\partial y}\right)\right]\right\} + S_{\text{i}}^{\text{E}} \tag{10}$$

Instead, for UEDGE, $\mathcal{E}[p_{\text{i}}] = \sum_{a\in\mathcal{S}^+} \mathcal{E}[p_a] + \mathcal{E}[p_{\text{D}}] + \mathcal{E}[p_{\text{Ne}}] = \sum_{a\in\mathcal{S}^{0+}} \mathcal{E}[p_a]$ reads:

$$\frac{\partial}{\partial t}\left(\frac{3}{2} T_{\text{i}} \sum_{a\in\mathcal{S}^{0+}} n_a\right) + \frac{\partial}{\partial x}\left[\frac{5}{2} T_{\text{i}} \sum_{a\in\mathcal{S}^{0+}}\left(n_a b_x V_{a\|}\right) - \kappa_{\text{i}x}^{\text{CL}} \frac{\partial T_{\text{i}}}{\partial x}\right] + \frac{\partial}{\partial y}\left[\frac{5}{2} T_{\text{i}} \sum_{a\in\mathcal{S}^{0+}}\left(n_a V_{a,n}^{\text{diff}}\right) - \kappa_{\text{i}}^{\text{AN}} \frac{\partial T_{\text{i}}}{\partial y}\right]$$
$$= \sum_{a\in\mathcal{S}^{0+}}\left[\mathbf{V}_a \cdot \boldsymbol{\nabla}\left(n_a T_{\text{i}}\right)\right] + \sum_{a\in\mathcal{S}^+}\left[\eta_{ax}^{\text{CL}}\left(\frac{\partial V_{a\|}}{\partial x}\right)^2 + \eta_a^{\text{AN}}\left(\frac{\partial V_{a\|}}{\partial y}\right)^2\right] + S_{\text{i}}^{\text{E}} \tag{11}$$

[6] With $\mathcal{F}_{\text{i}}^{\text{lim}}$ exclusively including either summations over all ion species or T_{i}, its value is ion-species independent.

implicitly assumed in [18], so that the resulting unified T_i has the neutrals species included as well, with[7] $T_\mathrm{D} = T_\mathrm{Ne} = T_\mathrm{i}$ [17, 31, 32].

By employing the relationship $\nabla\cdot(n_a T_\mathrm{i}\mathbf{V}_a) = n_a T_\mathrm{i}\nabla\cdot\mathbf{V}_a + \nabla(n_a T_\mathrm{i})\cdot\mathbf{V}_a$, the factor 3/2 in SOLPS-ITER x-convection term can be shown to equal UEDGE's 5/2 for the ion species. As per the viscous heating, SOLPS-ITER and UEDGE terms in $(\partial_x V_{a\parallel})^2$ and $(\partial_y V_{a\parallel})^2$ come from the double dot (Frobenius) product $\mathbf{\Pi}_a : \nabla\mathbf{V}_a$ involving the viscosity tensor $\mathbf{\Pi}_a$.

The different formulations[8] of the SOLEDGE2D contributions in $-b_x V_{a\parallel}\partial_x(n_\mathrm{e}T_\mathrm{e})$ and viscous heating stream from framing the equation in terms of *total* energy (equation (11) of [33]) and leveraging the definition of parallel electric field (equation (9) of [33]), consistently with appendix A of [32].

2.1.6. Electron energy equation. The temperature T_e is computed from equations (7)–(9) of [18] for the three codes, with cross-field anomalous electron heat diffusivity χ_e.

2.2. Neutral models

Section 2.2 of [18] and table 1 therein detail the treatment, within EIRENE [34], of the deuterogenic neutral species in $\mathcal{S}^0$ for SOLPS-ITER and SOLEDGE2D. The collection of reactions is here enlarged by including, equally in both SOLPS-ITER and SOLEDGE2D, ADAS-based neon reactions of EI[9] (EI: $\mathrm{e} + \mathrm{Ne} \rightarrow 2\mathrm{e} + \mathrm{Ne}^{1+}$) and RC[10] (RC: $\mathrm{e} + \mathrm{Ne}^{1+} \rightarrow \mathrm{Ne}$).

In all three codes (UEDGE included), the CX reactions $\mathrm{D} + \mathrm{Ne}^{z+} \rightarrow \mathrm{D}^+ + \mathrm{Ne}^{(z-1)+}$ are neglected, with such data however available in ADAS and employed by other edge codes [35].

In contrast to [18] and to SOLEDGE2D, SOLPS-ITER is here accounting for D/D, D/D_2 and D_2/D_2 collisions (via the BGK approximation [36]), included by default in SOLPS-ITER versions from the present 3.0.7 onwards.

With the simplified purely-diffusive neutral momentum equation commented in [18], neutral conduction is neglected in UEDGE and therefore does not enter equation (11) herein, neither in $\kappa_\mathrm{i}^\mathrm{CL}$ nor in $\kappa_\mathrm{i}^\mathrm{AN}$ (equation (8)). The subtle importance of neutral conduction is here only noted, as in [32], and instead addressed in [37].

3. Simulation setup

3.1. Scenario characterisation and comparison of code meshes

The same DTT magnetic equilibrium from [38] is analysed in the present work as in [18], which features a plasma current $I_\mathrm{p} = 5.5\,\mathrm{MA}$, with a magnetic field $B_0 = 6.0\,\mathrm{T}$ on axis. The same cross-field anomalous transport parameters (section 2) of [18] are used: $D^\mathrm{AN} = 0.05\,\mathrm{m^2\,s^{-1}}$, $\nu^\mathrm{AN} = 1.00\,\mathrm{m^2\,s^{-1}}$, and $\chi_\mathrm{e}^\mathrm{AN} = \chi_\mathrm{i}^\mathrm{AN} = 0.15\,\mathrm{m^2\,s^{-1}}$ in regards to particle, momentum, electron and ion heat diffusivity.

The field-aligned non-orthogonal quadrilateral meshes for the fluid plasma[11] (and fluid neutrals, for UEDGE), and EIRENE triangular grids of SOLPS-ITER and SOLEDGE2D for kinetic neutrals, are shown in figure 1.

As per [18], SOLPS-ITER and UEDGE fluid plasma (and fluid neutrals, for UEDGE) meshes are constituted by 96 poloidal and 36 radial cells. The spatial distribution along the two directions is non-uniform, with higher spatial resolution radially across the separatrix ($\leqslant$0.4 mm at outer mid-plane, OMP), and poloidally in the vicinity of the divertor targets ($\leqslant$1.0 mm). SOLEDGE2D mesh settings are chosen as to match similar figures.

A noteworthy addition compared to [18] is the neon puffing slot at the top of the divertor dome (PFR artificial boundary in UEDGE).

3.2. Boundary conditions and input parameters

With most of the boundary conditions (BCs) matching [18]'s, the present section highlights any differences in the settings, unless otherwise specified.

3.2.1. Plasma species. All the three codes implement a main-ion particle influx of $5\cdot10^{20}\,\mathrm{D^+\cdot s^{-1}}$ at the core boundary, and a zero-flux boundary condition for all the neon ionisation stages.

For each ion species ($a \in \mathcal{S}^+$), the BCs for the parallel ion momentum balance consist of zero parallel velocity $V_{a\parallel}$ at the core boundary. Instead, at the sheath (Sh) entrance, the velocity is (i) exactly equal to the *collective* sound speed in SOLPS-ITER: $V_{a\parallel}^\mathrm{Sh} = c_\mathrm{s} = \sqrt{\sum_a[n_a(Z_a T_\mathrm{e} + T_\mathrm{i})]\,/\sum_a(n_a m_a)}$ (divertor targets); (ii) greater or equal to the species-specific sound speed in SOLEDGE2D: $V_{a\parallel}^\mathrm{Sh} \geqslant c_{sa} = \sqrt{(Z_a T_\mathrm{e} + T_\mathrm{i})/m_a}$ (entire wall); (iii) exactly equal to the species-specific sound speed in UEDGE: $V_{a\parallel}^\mathrm{Sh} = c_{sa}$ (divertor targets). Ancillary investigations show how moving from (i) to (ii) in SOLPS-ITER does not lead to any appreciable change in the solution. Moreover, c_s and c_{sa} would differ by less than 10% in the near SOL in UEDGE (at least for D^+, whose momentum equation is solved for—section 2.1.3). The effect of the different formulations is therefore deemed uninfluential in the present case[12].

This full-power DTT scenario would have 45 MW of plasma heating. By assuming 10 MW to be radiated in the core (i.e. within the non-modelled core volume in figure 1) and 5 MW to be retained within the pedestal during the inter-ELM phase [14], $P_\mathrm{in} = 30$ MW crossing the core boundary into the modelled domain is imposed (with a 2:3 ion:electron

[7] As per section 2.2 of [18], neutral temperatures are herein intended as averages over the broad energy spectrum of neutral particles (section 1.8.2.4 of [27]).

[8] Erroneously reported in [18].

[9] From ADAS `scd96` (`plt96`) for the (energy-weighted) reactivity $\langle\sigma v\rangle$.

[10] From ADAS `acd96` (`prb96`) for the (energy-weighted) reactivity $\langle\sigma v\rangle$.

[11] SOLEDGE2D mesh has been built with the non-smoothed equilibrium, according to appendix A of [18].

[12] Conversely, [39] evidences that employing c_s instead of c_{sa} in presence of W erosion could lead to a pronounced over-estimation of the self-sputtering.

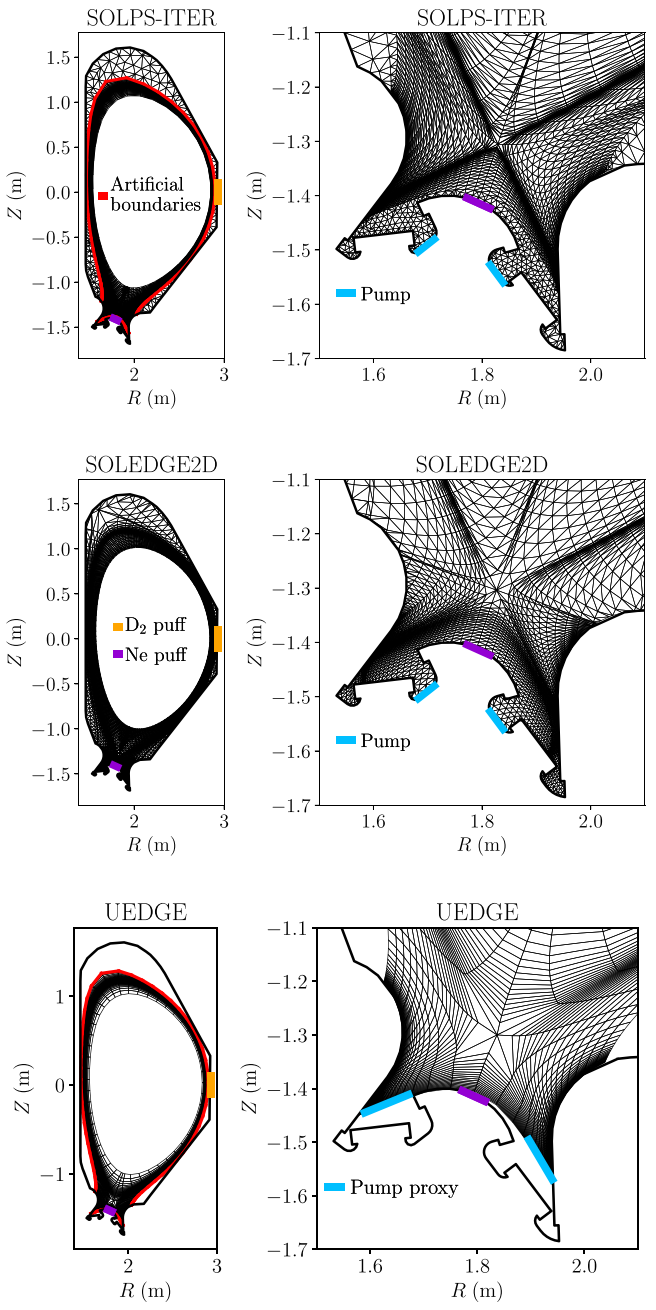


Figure 1. Meshes exploited by the three codes. From top to bottom in the left column: SOLPS-ITER (EIRENE), SOLEDGE2D (EIRENE), UEDGE. Zoomed-in divertor region in the right column. The SOLPS-ITER and UEDGE artificial boundaries of the plasma (and neutral, for UEDGE) domain are shown in red, the outer mid-plane D_2 (D in UEDGE) puffing port in amber, and the private flux region Ne puffing port in purple. The actual DTT divertor pump locations (light blue) on the vessel wall are considered by SOLPS-ITER and SOLEDGE2D, while UEDGE relies on artificial pumping surfaces on the private flux region boundary.

power split). At the wall surfaces, the electron energy balance settings equal those of [18] ($\gamma_e = 4.5$ in all codes). The ion heat flux flowing in the sheath (with $\gamma_a = \gamma_i = 2.5\ \forall a \in \mathcal{S}^+$ [18]) follows from $\Gamma_i^E = \sum_{a\in\mathcal{S}^+}[\gamma_i T_i + m_a(V_{a\|}^{Sh})^2/2]n_a V_{a\|}^{Sh}$ for SOLEDGE2D *total* ion energy formulation, and from $\Gamma_i^E = \gamma_i T_i c_s \sum_{a\in\mathcal{S}^+} n_a$ and $\Gamma_i^E = \gamma_i T_i \sum_{a\in\mathcal{S}^+} n_a c_{sa}$ in SOLPS-ITER and UEDGE *internal* ion energy equation, respectively.

3.2.2. Neutral species. With the aim of matching a core-compatible upstream density, alongside a PFC-friendly radiative mitigation, a common OMP separatrix density $n_e^{SEP} = 6\cdot10^{19}\,m^{-3}$ and total radiated power $P_{rad} = 20\,MW$ are simultaneously targeted, by manually tuning the control actuators of pumping albedo and neon puffing rate in feed-forward.

Two separate puffing slots for deuterogenic species and neon are accounted for. From the OMP wall (amber in figure 1), neutral deuterium is puffed at a fixed equivalent[13] atomic rate of $1\cdot10^{22}\,D\cdot s^{-1}$ in all the codes.

The pump albedo (<1) common to all the neutral species is independently tuned in the three codes, to reach $n_e^{SEP} = 6\cdot10^{19}\,m^{-3}$. During such tuning, the strength of neon puffing from the divertor dome in SOLPS-ITER and SOLEDGE2D, and from the PFR artificial boundary in UEDGE (purple in figure 1), is separately adjusted in the three codes to match $P_{rad} = 20\,MW$ the closest.

The temperature of the puffed gases is 0.03 eV (room temperature) in SOLPS-ITER and SOLEDGE2D, and local unified ion-neutral temperature in UEDGE (equation (11))—a crucial difference already assessed in [18] and re-considered in section 5.3.1.1 herein.

A unitary albedo is assumed on the remaining wall surfaces and any ion/neutral species is recycled as neutral (section 3.1 of [27]). TRIM-based fast and thermal reflection regulate the processes within EIRENE[14] occurring on actual wall boundaries (i.e. divertor targets in SOLPS-ITER, entire wall in SOLEDGE2D). Instead, with its default settings being in place, ions crossing the artificial radial boundaries in SOLPS-ITER (red in figure 1) are recycled as atoms (not molecules) at the local ion temperature, hence implicitly forcing fast reflection events fully retaining the incoming particle energy. Along the fore-mentioned artificial boundaries, the neutrals are thus treated by SOLPS-ITER as in UEDGE, though the latter leverages upon this approximation at the divertor targets also.

Last, SOLPS-ITER and SOLEDGE2D re-inject any kinetic neutrals reaching the core boundary as fully-stripped ions, while a zero neutral flux is imposed by UEDGE at the core boundary—such settings were equally employed in [18] with no noticeable effect.

4. Results

Using the edge plasma scenario and code setups of section 3, the three codes are run to convergence, assessed with the criteria defined in [18].

[13] The rate is actually $5\cdot10^{21}\,D_2\cdot s^{-1}$ in EIRENE.

[14] Among other parameters, EIRENE reflection is a function of the `ERMIN` parameter, threshold below which the reflection is forced to be thermal [34]. However, while `ERMIN` = 1 eV in SOLPS-ITER by default, `ERMIN` = 2 eV in SOLEDGE2D, a difference not analysed in the present work but potentially non-negligible in low-temperature detached regimes.

Table 1. Highlights of the baseline results of the three codes. Scrape-off layer (SOL) data within 1 mm of the separatrix (SEP) are considered to compute each decay length (λ) via an exponential fit at outer mid-plane (OMP).

Region	Quantity (units)	SOLPS-ITER	SOLEDGE2D	UEDGE	Δ
OMP	n_e 3.0 cm inside SEP (m^{-3})	$9.17 \cdot 10^{19}$	$9.67 \cdot 10^{19}$	$14.23 \cdot 10^{19}$	5%–43%
	n_{D+} 3.0 cm inside SEP (m^{-3})	$5.60 \cdot 10^{19}$	$3.82 \cdot 10^{19}$	$13.93 \cdot 10^{19}$	38%–114%
	T_e 3.0 cm inside SEP (keV)	5.04	5.25	3.62	4%–37%
	T_i 3.0 cm inside SEP (keV)	5.31	9.97	2.82	61%–112%
	p_e 3.0 cm inside SEP (kPa)	73.9	81.2	82.4	2%–11%
	p_{D+} 3.0 cm inside SEP (kPa)	47.6	61.0	62.9	3%–28%
	Z_{eff} 3.0 cm inside SEP (−)	4.50	7.23	1.17	47%–144%
	n_e at SEP (m^{-3})	$5.90 \cdot 10^{19}$	$5.94 \cdot 10^{19}$	$5.99 \cdot 10^{19}$	0%–1%
	n_{D+} at SEP (m^{-3})	$2.95 \cdot 10^{19}$	$0.91 \cdot 10^{19}$	$4.96 \cdot 10^{19}$	51%–138%
	T_e at SEP (eV)	312.1	299.9	240.0	4%–26%
	T_i at SEP (eV)	1059.2	1490.6	631.3	34%–81%
	p_e at SEP (kPa)	2.91	3.14	2.71	7%-15%
	p_{D+} at SEP (kPa)	4.98	2.34	5.26	6%–77%
	Z_{eff} at SEP (−)	5.25	7.28	2.21	33%–107%
	SOL n_e decay length (mm)	11.1	12.7	8.6	13%–38%
	SOL n_{D+} decay length (mm)	10.4	4.5	8.3	22%–79%
	SOL T_e decay length (mm)	2.0	1.6	1.7	6%–22%
	SOL T_i decay length (mm)	7.6	2.1	8.1	6%–118%
	SOL p_e decay length (mm)	1.7	1.4	1.4	0%–19%
	SOL p_{D+} decay length (mm)	4.4	1.5	4.1	7%–98%
Inner	Peak n_e (m^{-3})	$9.38 \cdot 10^{21}$	$4.48 \cdot 10^{21}$	$6.34 \cdot 10^{21}$	34%–71%
	Peak T_e (eV)	70.9	59.8	79.0	11%–28%
	Peak T_i (eV)	386.8	180.5	171.2	5%–77%
	Peak $q_\perp$ ($MW \cdot m^{-2}$)	8.8	5.2	5.3	23%–78%
	T_e 3.5 cm in PFR (eV)	0.09	1.60	0.60	91%–179%
	T_i 3.5 cm in PFR (eV)	0.09	1.71	0.84	69%–181%
Outer	Peak n_e (m^{-3})	$13.20 \cdot 10^{21}$	$3.25 \cdot 10^{21}$	$19.00 \cdot 10^{21}$	36%–142%
	Peak T_e (eV)	110.3	93.9	111.3	1%–17%
	Peak T_i (eV)	422.8	274.5	265.9	3%–46%
	Peak $q_\perp$ ($MW \cdot m^{-2}$)	29.2	11.1	76.6	88%–178%
	T_e (eV) 3.5 cm in PFR	0.18	2.08	0.66	104%–168%
	T_i (eV) 3.5 cm in PFR	0.18	3.06	0.78	119%–178%

All the codes achieve the targeted n_e^{SEP} within 1%. Nevertheless, the target $P_{rad} = 20$ MW could not be unanimously reached, with resulting combinations of: $P_{rad} = 14.7$ MW and $4 \cdot 10^{19}$ Ne $\cdot s^{-1}$ puff in SOLPS-ITER; $P_{rad} = 20.5$ MW and $1 \cdot 10^{20}$ Ne $\cdot s^{-1}$ puff in SOLEDGE2D; $P_{rad} = 18.5$ MW and $6 \cdot 10^{19}$ Ne $\cdot s^{-1}$ puff in UEDGE.

The inability to achieve a closer match for n_e^{SEP} and P_{rad} follows from pronounced non-linearities observed in these strongly-seeded scenarios: some codes yield more deeply detached states than others—an exemplifying instance being illustrated in section 5.3.5.2, where SOLPS-ITER reaches $P_{rad} \sim 20$ MW with SOLEDGE2D-like settings.

Other key quantities of the simulations results are summarised in table 1, with the relative difference of the outcomes Δ being defined by equation (18) in [18]. More in-depth descriptions for the OMP, divertor targets and divertor volume are given in sections 4.1–4.3, respectively.

4.1. Outer mid-plane: 1D profiles

One-dimensional plasma profiles taken at OMP are shown in figure 2. Electron density n_e and temperature T_e show an excellent match (within 5% throughout the core) in SOLPS-ITER and SOLEDGE2D, whereas the UEDGE profile deviates from the other two—a trend previously observed in [18]. In this work, this discrepancy is significantly more pronounced: the UEDGE electron density (temperature) lies up to 43% (37%) above (below) SOLPS-ITER's and SOLEDGE2D's in the core region, conversely in the SOL. As in [18], the same observation holds for the UEDGE main ion density n_{D+} (unified ion temperature T_i), but to an even greater extent of being a factor 2.5 higher (1.9 lower) in the core compared to SOLPS-ITER's.

The agreement in the electron channel between SOLPS-ITER and SOLEDGE2D is lost for the ions, for which the two code's predictions differ up to 38% and 61% in the

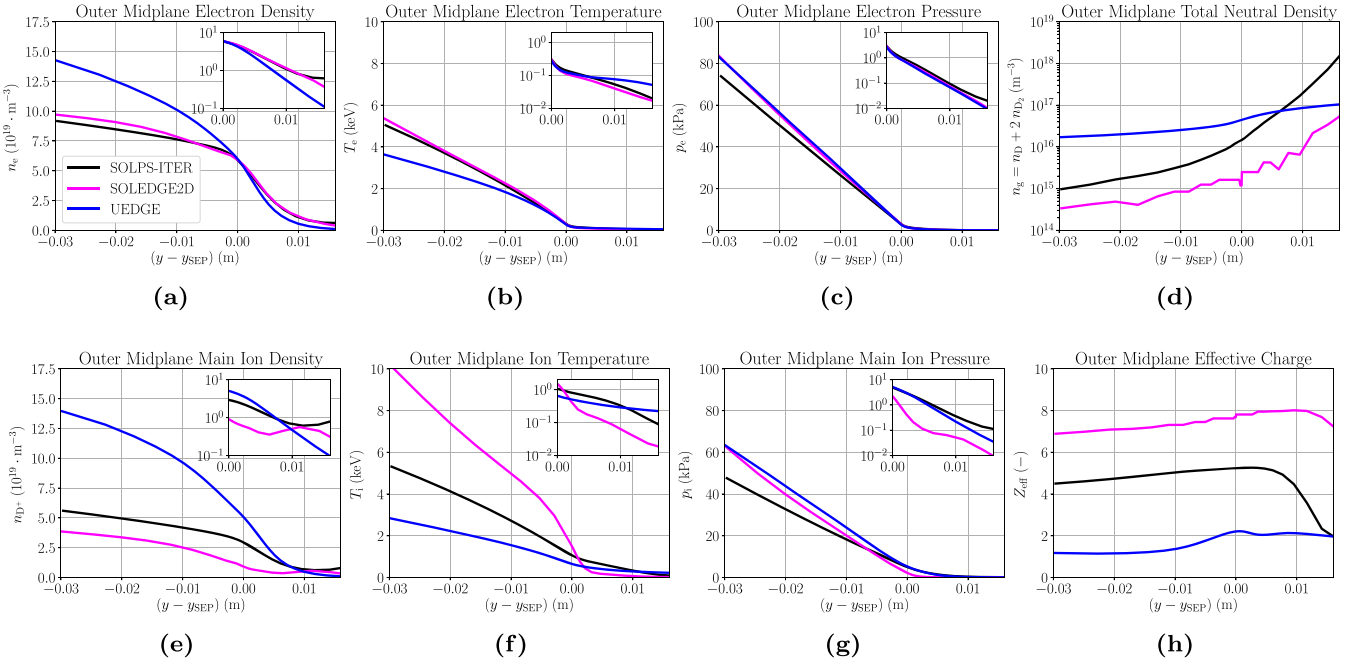


Figure 2. Plasma and neutral profiles at outer mid-plane (separatrix at $y - y_{SEP} = 0$). The insets show the profiles in logarithmic scale.

core main ion density and unified ion temperature, respectively. Moreover, a strong qualitative mismatch arises in the edge main ion density, featuring disparate non-monotonic behaviours (inset of figure 2(e)), and in the ion temperature in the core, where SOLEDGE2D shows variable gradients despite the constant radial transport coefficients employed (section 3.1).

Given the interactions between $\mathcal{S}^+$ and $\mathcal{S}^0$, an accompanying disagreement in the total deuterium neutral density $n_g = n_D + 2\,n_{D_2}$ follows. SOLEDGE2D prediction in the far SOL lies one order of magnitude above SOLPS-ITER's, which, in turn, is one order of magnitude larger than UEDGE's. Conversely, at the core boundary in UEDGE, n_g is an order of magnitude larger than that of the other two codes.

In spite of the differences in plasma densities and temperatures, the electron pressure p_e is verified to show the expected agreement among the three codes all throughout the OMP. Nevertheless, the same does not apply for the main ion pressure $p_{D^+} = n_{D^+} T_i$, owing to the substantial differences in n_{D^+} and T_i: while the values in the core plasma agree within 1%–27%, SOLEDGE2D predicts a main ion pressure strongly different from the separatrix onwards, an order of magnitude lower than that of the other two codes.

Notably, the relationships of $1/\lambda_{p_e} = 1/\lambda_{T_e} + 1/\lambda_{n_e}$ and $1/\lambda_{p_{D^+}} = 1/\lambda_{T_i} + 1/\lambda_{n_{D^+}}$ (equation (4.18) of [27]) are precisely satisfied in the present case, likely because of the constant transport coefficients assumed. The only exception is $\lambda_{p_{D^+}} = 1.5$ mm in SOLEDGE2D, with 4.4 mm predicted by [27] and accurately matched by SOLPS-ITER and UEDGE.

Of central interest in edge and core-edge plasma studies to assess the plasma pollution and fuel dilution is $Z_{eff} = \sum_{a \in \mathcal{S}^+} n_a Z_a^2 / n_e$. Profiles of Z_{eff} at OMP (figure 2(h)) show large discrepancies among the three codes, SOLEDGE2D predicting a Z_{eff} up to six times larger than UEDGE's in the core plasma, and SOLPS-ITER prediction sitting halfway through, this overall not correlating with the neon puffing strength in the three codes. A better agreement, at least between SOLPS-ITER and UEDGE, is recovered in the far SOL.

4.2. Divertor region: 1D profiles

Profiles of key plasma quantities along the divertor targets are shown in figure 3. For the attached SOL regions ($T_e > 5$ eV), most of the differences at the divertor targets are related to the upstream behaviour: e.g. the ion temperature predicted by SOLPS-ITER in the near SOL and UEDGE electron temperature in the far SOL are higher than those of the other two codes.

Similarly to [18], substantial disagreement emerges in the electron density at the inner target (a difference of a factor 2.1) and at the outer target (SOLEDGE2D outcome lower by a factor 4.1 and 5.8 with respect to SOLPS-ITER's and UEDGE's, respectively). The main ion density profile matches the electron's by virtue of $Z_{eff} = 1$ all throughout the near SOL at the target plates (figure 5)—hence not shown.

Strike-points are detached at both inner and outer targets, but the position where the onset of plasma re-attachment occurs varies: for an agreement within 6 mm at the outer target (onset placed at $(y - y_{SP}) \sim 10$ mm, as evidenced by the rise in electron and ion temperatures), plasma temperatures at the inner target are predicted by SOLPS-ITER to rise 23 mm closer to the strike point than the other codes. Overall,

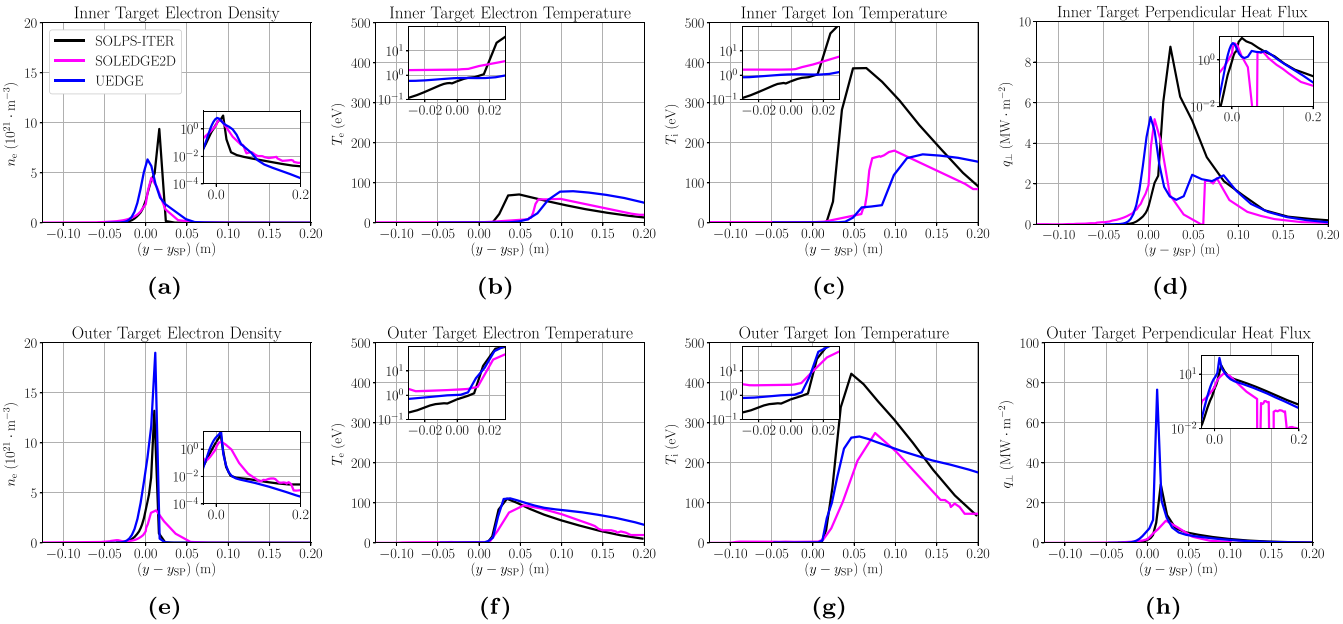


Figure 3. Plasma profiles at the inner and outer divertor targets (strike point at $y - y_{SP} = 0$). Perpendicular heat fluxes are pictured with different vertical axis to improve readability. The insets show the profiles in logarithmic scale.

this behaviour is consistent with a significant in-out symmetry of the plasma profiles in SOLPS-ITER, instead absent in SOLEDGE2D and UEDGE.

The perpendicular plasma[15] heat flux $q_\perp$ and the corresponding integral power at the outer target feature a dramatic quantitative disparity (up to a factor 7 for the peak flux and 2 for the power). This discrepancy in the profile is progressively reduced as the radial distance increases. At the inner target, the results of SOLEDGE2D and UEDGE are in excellent quantitative agreement (peak heat flux within 1%) and in predicting a doubly-peaking profile, in stark opposition to SOLPS-ITER bell-shaped Eich-ian behaviour [1], integrating to twice as much power as SOLEDGE2D.

4.3. Divertor region: 2D maps

Two dimensional views of the divertor volume are pictured in figure 4. The deuterogenic total density n_g closely resembles its counterpart in [18]: the maximum density in SOLPS-ITER inner target agrees with UEDGE's within 11%, while SOLEDGE2D prediction is one order of magnitude lower than SOLPS-ITER's. Disagreement at the outer target is found: SOLPS-ITER's density is a factor 3 higher compared to UEDGE's, and two orders of magnitude larger than in SOLEDGE2D. Although the in-out asymmetries of the distributions in the PFR are here milder, UEDGE still shows the highest in-out balance ($7.0 \cdot 10^{21}\,\mathrm{m}^{-3}$ in, and $1.5 \cdot 10^{22}\,\mathrm{m}^{-3}$ out), with SOLPS-ITER (once more developing spurious gradient along the PFR artificial radial boundary) and SOLEDGE2D marginally peaking in the inboard.

Stronger asymmetries are observed in the neon density distribution n_{Ne}, with higher values in the inboard in SOLPS-ITER and SOLEDGE2D; UEDGE presents a wider high-density region around the inner strike point and, crucially, at the pump ducts. Quantitatively, UEDGE features the highest n_{Ne}, followed by SOLEDGE2D (a factor 1.8 lower), and by SOLPS-ITER (a factor 4.4 lower, with no spurious gradients), which does not correlate with the different neon puffing rates.

An important disagreement is observed for Z_{eff}, not only at the OMP (figure 2(h)), but throughout the entire divertor volume (figure 5), once again not correlating with neon injection rates. Although $Z_{eff} \sim 1$ in the near SOL in all the three codes, the radial extent of this region in SOLEDGE2D far outstretches SOLPS-ITER's and UEDGE's. SOLPS-ITER and UEDGE do show an analogous Z_{eff} inboard peaking, though jeopardised by poor quantitative agreement (only within a factor 1.5). SOLEDGE2D does not feature any such peaking, nor the intuitive drop of Z_{eff} in the far, cold SOL where RC of high-ionisation stages should be primed.

The spatial distribution of the total radiation source S_{tot}^{rad} (both deuterogenic and impurity-driven) of figure 6 is satisfactorily matched by the codes, in the regions of high emission. A characteristic peaking along the divertor legs [10, 40] is noted, in SOLPS-ITER protruding up to the X-point. Quantitatively, the maximum values of the three radiation distributions are found at $0.37 \cdot 10^{10}\,\mathrm{W \cdot m^{-3}}$, $0.43 \cdot 10^{10}\,\mathrm{W \cdot m^{-3}}$, and $1.11 \cdot 10^{10}\,\mathrm{W \cdot m^{-3}}$, respectively, and they overall integrate to 14.7 MW, 20.5 MW, and 18.5 MW.

5. Discussion

Throughout the following, unless specified otherwise, we shall denote by $\langle \xi_a \rangle$ the value of an ion-species-specific variable ξ_a

[15] Hence neglecting contributions from neutrals and radiation.

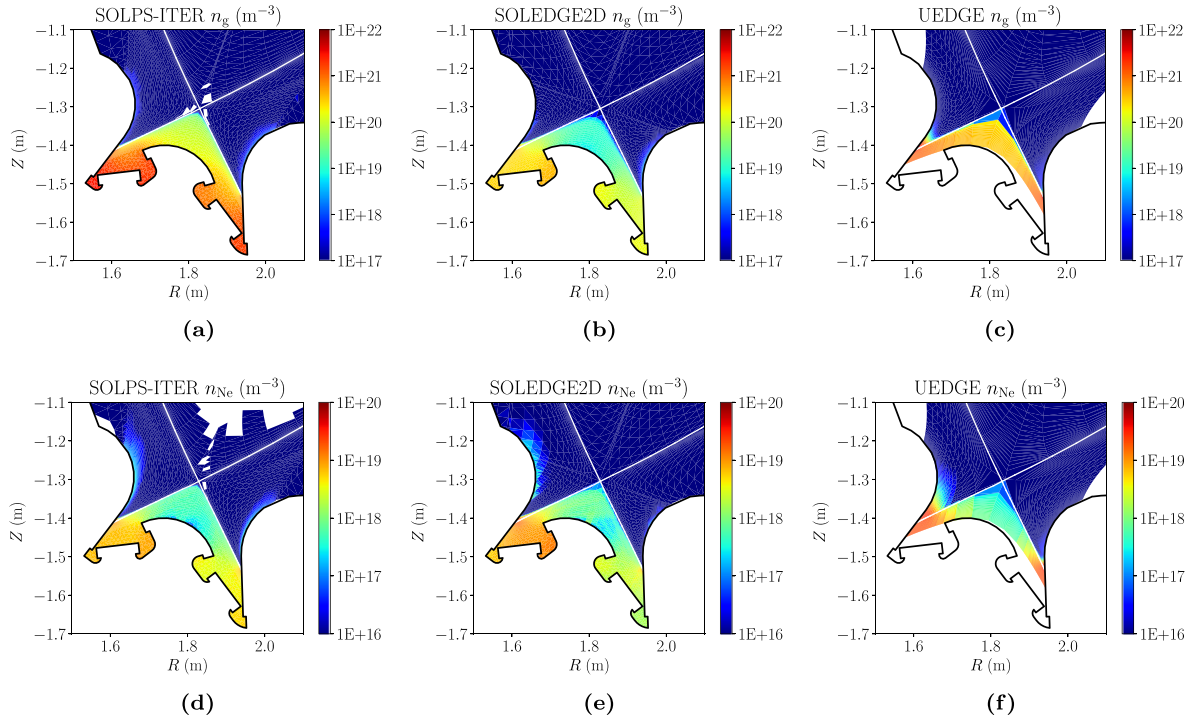


Figure 4. Deuterogenic total density maps in the divertor (first row): $n_g = n_D + 2\,n_{D_2}$ for SOLPS-ITER (*a*) and SOLEDGE2D (*b*), $n_g = n_D$ for UEDGE (*c*). Neutral neon density maps in the divertor (second row): SOLPS-ITER (*d*), SOLEDGE2D (*e*), UEDGE (*f*). Separatrix pictured in white.

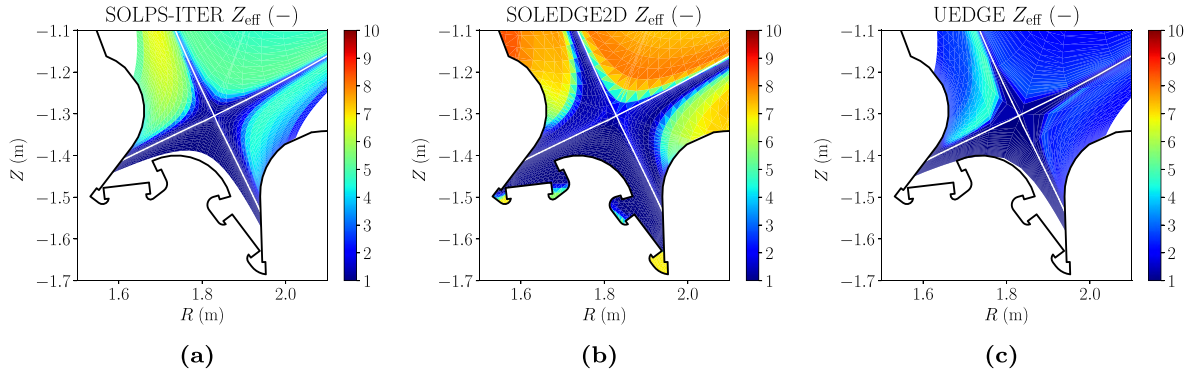


Figure 5. Effective charge distribution Z_{eff} in the divertor for SOLPS-ITER (*a*), SOLEDGE2D (*b*), and UEDGE (*c*).

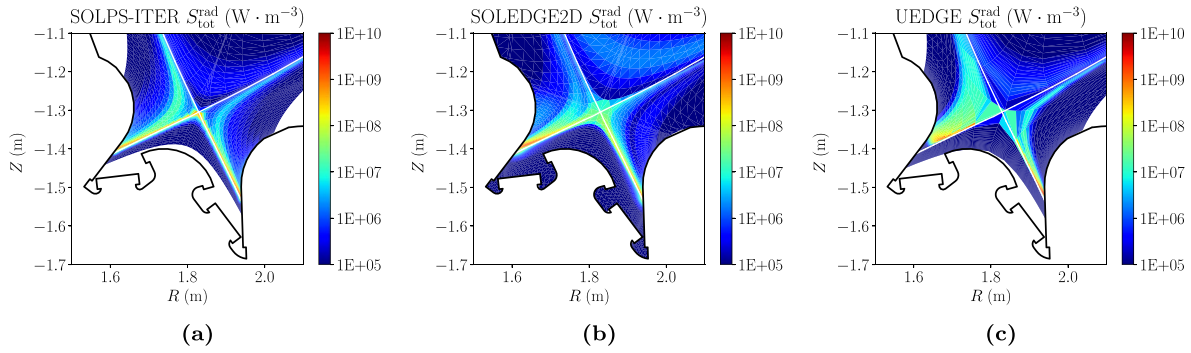


Figure 6. Distribution of total radiated power S_{tot}^{rad} in the divertor for SOLPS-ITER (*a*), SOLEDGE2D (*b*), and UEDGE (*c*).

($a \in \mathcal{S}^+$) averaged over all the ion species with weights $w_a = Z_a n_a / n_e$, such that $\langle \xi_a \rangle = \sum_a w_a \xi_a$.

5.1. Validity of impurity model assumptions

5.1.1. Unified ion temperature. The appropriateness of assuming an instantaneous thermal equilibration between different ion species ($T_a = T_i \; \forall a$, section 2.1.5) is assessed by verifying whether the average collision time of ion species a ($\tau_{ca} = \langle \tau_{ab}^{SI} \rangle$ from equation (3), averaged over $b \in \mathcal{S}^+$) is shorter than the cell-specific residence time τ_{ra}, according to the here proposed definitions:

$$\begin{aligned} \tau_{ra}^{\parallel} &= \max\left\{\Delta x;\, \min\left\{\frac{T_i}{|\partial_x T_i|};\, L_{ax}\right\}\right\} \cdot \frac{1}{|V_{a\parallel}|} \frac{||\mathbf{B}||}{B_x} \\ \tau_{ra}^{y} &= \max\left\{\Delta y;\, \min\left\{\frac{T_i}{|\partial_y T_i|};\, L_{ay}\right\}\right\} \cdot \frac{1}{|V_{ay,n}^{diff}|} \\ \Rightarrow \tau_{ra} &= \min\left\{\tau_{ra}^{\parallel};\, \tau_{ra}^{y}\right\} \end{aligned} \tag{12}$$

In equation (12): Δx and Δy are the cell poloidal x and radial y lengths, respectively (i.e. the smallest possible spatial scale in the present meshes, hence $\max\{\cdot\}$); the characteristic length scale of ion temperature variation[16] along x and y are represented by $T_i/|\partial_x T_i|$ ($T_i/|\partial_y T_i|$); L_{ax} and L_{ay} are the distances from a give cell to, respectively, a divertor target and radial boundary (i.e. the longest possible space scale, hence $\min\{\cdot\}$), with the direction of integration determined by $\text{sign}\{V_{ax}\}$ and $\text{sign}\{V_{ay,n}^{diff}\}$; finally, $||\mathbf{B}||/B_x$ identifies the projector from the poloidal (x) to parallel ($\parallel$) direction.

In support of the analysis, the normalised metric $\Delta\tau_a = (\tau_{ca} - \tau_{ra})/(\tau_{ca} + \tau_{ra})$ is introduced, such that $\Delta\tau_a \geqslant 0 \Leftrightarrow \tau_{ca} \geqslant \tau_{ra}$ implies that the assumption of a unified ion temperature is ill-posed, and well-posed where $\Delta\tau_a < 0 \Leftrightarrow \tau_{ca} < \tau_{ra}$. According to its weighted-average over all ion species, $\Delta\tau = \langle \Delta\tau_a \rangle$, the unified ion temperature is appropriate (blue in figure 7) for SOLPS-ITER and UEDGE throughout the core, for the deuterium-dominated collisional plasma of the detached near-SOL and of the PFR. It is instead invalid (white-red in figure 7) in the far SOL where, crucially, Z_{eff} increases and impurity presence is noticeable (figure 5), affecting the entire SOL poloidal extent in UEDGE, only the near-target regions in SOLPS-ITER (as suggested by [27]).

It should be noted that equation (12) implicitly neglects non-local effects, for ∇T_i being computed between neighbouring cells, instead of leveraging on integral averages along the x and y directions. Accounting for non-locality goes beyond the purpose of the present section, as does the quantification of the model error due to the adoption of the unified ion temperature approximation, uniquely possible in SOLEDGE2D by separately solving ion-species-specific energy equations (section 2.1.5).

[16] Metric coefficients [41] are neglected in the differentiation process for the sake of simplicity.

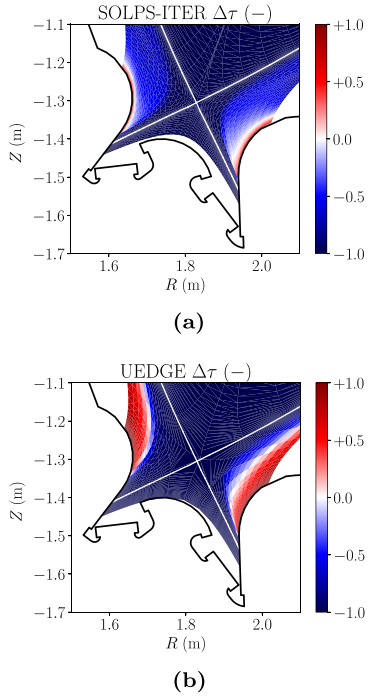


Figure 7. Applicability of the unified ion temperature approximation in SOLPS-ITER (*a*) and UEDGE (*b*): well-posed where blue, ill-posed where white-red (see section 5.1.1 for $\Delta\tau$ definition).

5.1.2. Trace impurity approximation. Strongly-seeded edge plasma scenarios can violate the applicability of the trace impurity approximation—the present case providing one such instance. This is exemplified by figure 8, where 2D plots of Z_0 show that the TIA condition $Z_0 \ll 1$ (equation (1)) is largely violated in SOLEDGE2D (almost exclusively due to Ne^{8+}, Ne^{9+} and Ne^{10+}). Similar observations hold, albeit up to a lower extent, in SOLPS-ITER and UEDGE, in the latter case even despite the significantly lower values of Z_{eff} (section 5.3.4.2).

However, while SOLPS-ITER and SOLEDGE2D can employ the Zhdanov formulation [42], compatible with any impurity content (i.e. $\forall Z_0$, non TIA-based), UEDGE does not offer such option. The Zhdanov closure was disabled in SOLPS-ITER and SOLEDGE2D in favour of Braginskii's for the sake of consistency (section 2.1.3).

The Z_0-dependent terms in equations (5) and (6) are impacted in UEDGE upon violation of TIA: this suggests the possibility to obtain improved code performance by implementing further options in the code.

Also worthwhile pursuing would be a cross-code comparison between SOLPS-ITER and SOLEDGE2D with extrinsic impurities and with their own implementations of the Zhdanov formulation ([33, 43], respectively). Nonetheless, the complications arising from the necessary inclusion of currents (at least in SOLPS-ITER) might force a preliminary study in the fashion of the un-seeded [18], before proceeding any further.

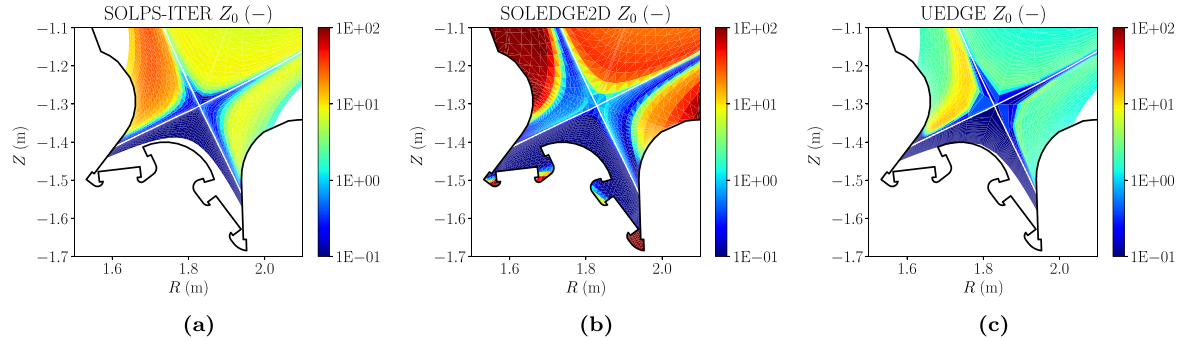


Figure 8. Applicability of the trace impurity approximation (TIA) for SOLPS-ITER (*a*), SOLEDGE2D (*b*), and UEDGE (*c*), verified only where $Z_0 = \sum_z n_z Z_z^2 / n_{\mathrm{D}^+} \ll 1$.

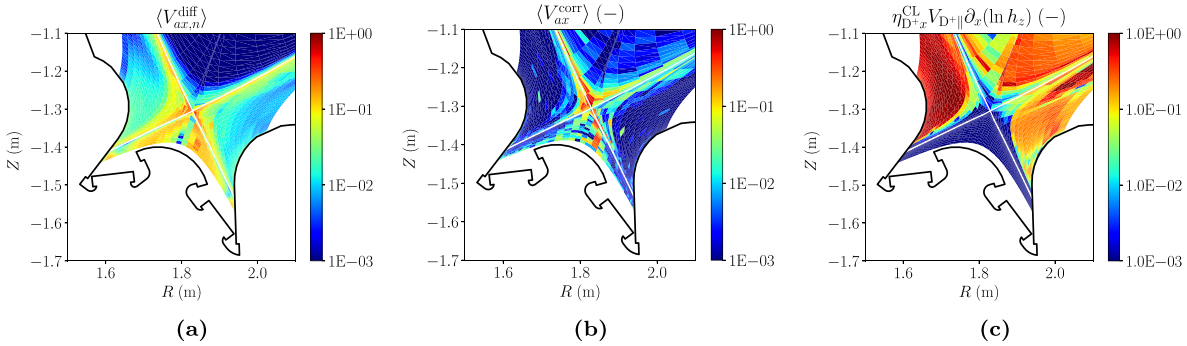


Figure 9. Relative importance of SOLPS-ITER extra terms (averaged over ion species, details in section 5.2.1) of diffusive velocity (*a*), Rhie-Chow correction velocity (*b*), and geometry-related term in the momentum equation (*c*)—non-zero for D^+ only. The presence of (*a*) and (*b*) is also particularly noticeable at outer mid-plane.

5.2. *Intrinsic differences in plasma equations*

5.2.1. Extra terms in SOLPS-ITER plasma equations. The additional poloidal terms present in the SOLPS-ITER equations, not included neither in SOLEDGE2D nor in UEDGE, deserve a dedicated assessment, as accomplished in [18]. Their relative importance is computed according to section 5.1 of [18] ($\mathcal{L}^1$ norm), averaged over the ion species $\langle \cdot \rangle$ where required.

The SOLPS-ITER equations contain the convective terms[17] in $V_{ax,n}^{\mathrm{diff}}$ and Rhie-Chow V_{ax}^{corr} (to avoid checkerboard instability), plus a geometry-related term $\eta_{\mathrm{D}^+x}^{\mathrm{CL}} V_{\mathrm{D}^+\parallel} \partial_x (\ln h_z)$ (exclusively in the main ion momentum equation [15]). Figure 9 shows plots for the relative importance of these quantities (normalised to $|\langle V_{ax,n}^{\mathrm{diff}} \rangle| + |\langle V_{ax}^{\mathrm{corr}} \rangle| + |\langle V_{ax} \rangle|$). The results evince spatial-average figures of 3.8%, 2.5%, and 15% throughout the domain, respectively, indicating generally low importance, just as in [18]. Nonetheless, peaks of 50%–100% in the role played by $\langle V_{ax,n}^{\mathrm{diff}} \rangle$ and $\langle V_{ax}^{\mathrm{corr}} \rangle$ are attained in the regions of the OMP (not shown), at the X-point, and in the near-SOL region along the divertor legs for $\langle V_{ax,n}^{\mathrm{diff}} \rangle$. Instead, in spite of its noticeable presence all throughout the far SOL, the relevance of $\eta_{\mathrm{D}^+x}^{\mathrm{CL}} V_{\mathrm{D}^+\parallel} \partial_x (\ln h_z)$ is negligible along the divertor legs.

Anomalous transport terms along the x direction are also added[18] on physical grounds in SOLPS-ITER, for the nature of turbulence being 3D, hence affecting both the poloidal (x) and the radial (y) directions [32, 44]. The relative importance of the three x-directed anomalous transport coefficients $\langle \eta_a^{\mathrm{AN}} \rangle$, $\kappa_{\mathrm{ex}}^{\mathrm{AN}}$ and $\kappa_{\mathrm{ix}}^{\mathrm{AN}}$ (in equations (2) and (7) of [18] and in equation (9) herein, respectively) is depicted in figure 10 in the computational space [45], providing an alternative representation which avoids the shortcomings of a physical-space-centred visualisation. The presence of $\langle \eta_a^{\mathrm{AN}} \rangle$, $\kappa_{\mathrm{ex}}^{\mathrm{AN}}$, and $\kappa_{\mathrm{ix}}^{\mathrm{AN}}$ is mostly negligible, in fact spatially-averaging 5.5%, 0.8%, and 1.1% respectively in the domain. However, values in excess of 40% at the detachment front are present in all the three cases, in particular at the outer target (East boundary in figure 10) where the plasma temperature drops; this leads to conjecturing a role being played by turbulent transport in detached conditions—an area of ongoing research [46, 47]. Discarding these contributions would be possible in SOLPS-ITER, and should be accomplished to shed light on their actual role, but this is not here performed.

5.2.2. Collision times. Under the assumption $T_{\mathrm{e}}/m_{\mathrm{e}} \gg T_{\mathrm{i}}/m_b$, a direct comparison of the characteristic collision times in SOLPS-ITER's (SI) equation (3) and SOLEDGE2D's (SE)

[17] The factor 5/3 rescaling $V_{ax,n}^{\mathrm{diff}}$ in the energy equations is neglected for the sake of simplicity, providing a mere marginal correction.

[18] With D^{AN} entering the equations via $V_{ax,n}^{\mathrm{diff}}$.

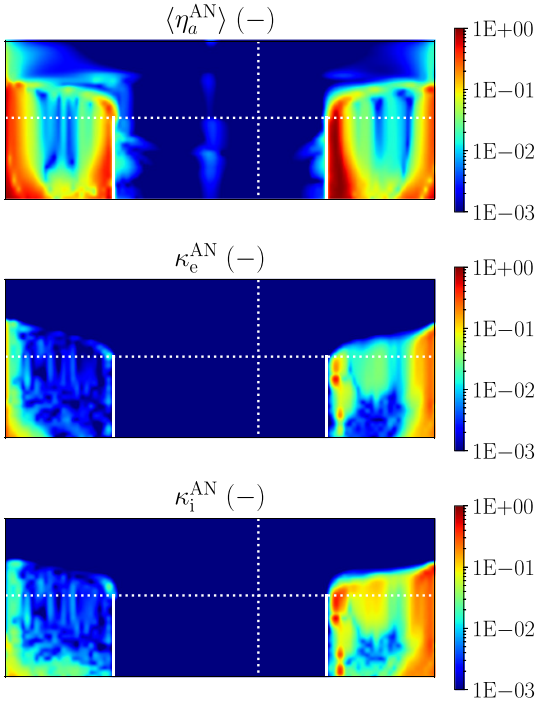


Figure 10. Relative importance of momentum (top, averaged over ion species), electron (centre) and ion (bottom) anomalous transport coefficient along the x direction in SOLPS-ITER computational mesh. The white vertical dotted line identifies the location of the outer mid-plane. The reader is referred to figure 18 of [45] for instructions on the interpretation of the computational mesh.

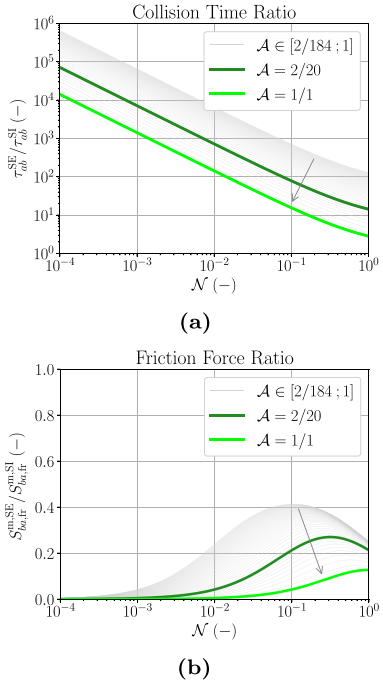


Figure 11. Ratio between SOLEDGE2D (SE) and SOLPS-ITER (SI) ion–ion collision time τ_{ab} (a) and ion–ion friction force $S_{ba,\mathrm{fr}}^{\mathrm{m}}$ (b) as a function of density ratio $\mathcal{N}$ (with values representative of the entire domain, excluding deep core and far PFR) and for various mass ratios $\mathcal{A}$ (details in section 5.2.2). Lime: neon/neon (1/1, different ionisation stages and neglecting the electron mass). Green: deuterium/neon (2/20). Grey: $\mathcal{A} \in [2/184\,;1]$ spanning combinations of masses down to deuterium/tungsten (2/184) with the grey arrow identifying the direction of increasing $\mathcal{A}$.

equation (5) yields:

$$\frac{\tau_{eb}^{\mathrm{SE}}}{\tau_{eb}^{\mathrm{SI}}} = \frac{1}{2}\frac{n_{\mathrm{e}}+n_b}{n_{\mathrm{e}}}\frac{m_b}{m_{\mathrm{e}}} \gg 1 \;\forall b \in \mathcal{S}^+ \tag{13}$$

for electron–ion collisions. In SOLEDGE2D, τ_{eb} is a factor $\sim m_b/m_{\mathrm{e}}$ (i.e. 3 to 5 orders of magnitude) larger than in SOLPS-ITER. This would be associated to a proportional mismatch in energy equipartition, if figuring as such.

Conversely, the ratio between τ_{ab}^{SE} and τ_{ab}^{SI} for ion–ion collisions reads:

$$\begin{aligned}\frac{\tau_{ab}^{\mathrm{SE}}}{\tau_{ab}^{\mathrm{SI}}} &= \frac{\sqrt{2}}{2}\frac{n_a+n_b}{n_a}\frac{(m_a+m_b)^2}{m_a m_b} = \\ &= \frac{\sqrt{2}}{2}\frac{1+\mathcal{N}}{\mathcal{N}}\frac{(1+\mathcal{A})^2}{\mathcal{A}}\end{aligned} \tag{14}$$

where $\mathcal{N} = \min\{n_a;n_b\}/\max\{n_a;n_b\} \leqslant 1\;\forall a,b$ and $\mathcal{A} = \min\{A_a;A_b\}/\max\{A_a;A_b\} \leqslant 1\;\forall a,b$ (A being the atomic mass number). This ratio is pictured in figure 11(a): we note that $\tau_{eb}^{\mathrm{SE}}/\tau_{eb}^{\mathrm{SI}} \geqslant 2.8\;\forall a,b \in \mathcal{S}^+$, and $\tau_{ab}^{\mathrm{SE}}/\tau_{ab}^{\mathrm{SI}} \sim \mathcal{N}^{-1}$. This dependency is not of concern per se, for any inter-species interaction being suppressed at low $\mathcal{N}$, i.e. when substantial disparity in densities exists (section 5.2.3.1). But consequences of the above on the momentum balance are further investigated in section 5.2.3.1.

Last, comparing SOLPS-ITER (SI) and UEDGE (UE) characteristic collision times between main and impurity ions in equation (7) yields:

$$\frac{\tau_{\mathrm{pz}}^{\mathrm{UE}}}{\tau_{\mathrm{pz}}^{\mathrm{SI}}} = \sqrt{\frac{2\mu_{\mathrm{pz}}}{m_{\mathrm{p}}}} \sim \sqrt{2} \tag{15}$$

where the simplification holds under the assumption of $m_z \gg m_{\mathrm{D}^+}$ within the TIA framework [28, 43].

5.2.3. *Ion momentum equations.*

5.2.3.1. Incongruities in the momentum equation of SOLPS-ITER and SOLEDGE2D. Taking the ratio of equations (4) and (2) for SOLEDGE2D and SOLPS-ITER ion–ion friction force ($a,b \in \mathcal{S}^+$) yields[19]:

$$\begin{aligned}\frac{S_{ba,\mathrm{fr}}^{\mathrm{m,SE}}}{S_{ba,\mathrm{fr}}^{\mathrm{m,SI}}} &= 0.51 \cdot \frac{m_a^2+m_b^2}{m_a+m_b}\frac{1}{n_a m_b + n_b m_a}\frac{n_a n_b}{n_a+n_b} \\ &= 0.51 \cdot \frac{1+\mathcal{A}^2}{1+\mathcal{A}}\frac{\mathcal{N}}{\mathcal{A}+\mathcal{N}}\frac{1}{1+\mathcal{N}}\end{aligned} \tag{16}$$

[19] If `b2sigp_style` = 2 in SOLPS-ITER, $S_{ba,\mathrm{fr}}^{\mathrm{m}}$ gets rescaled by an impurity-concentration-dependent factor. For concentrations spanning the range $[10^{-5};10^{0}]$, such factor attains value comprised within $(0.3;1.6)$. The conclusions of the present discussion would therefore hold irrespective of the particular `b2sigp_style`, with only the numerical factor slightly changing.

which suggests the existence of a fundamental discrepancy in the two formulations, related to (though not exclusively explained by) the different ion–ion collision times (section 5.2.2).

The ratio $S^{\mathrm{m,SE}}_{ba,\mathrm{fr}}/S^{\mathrm{m,SI}}_{ba,\mathrm{fr}}$ (figure 11(*b*) shows how SOLEDGE2D friction force is always more than 60% smaller than SOLPS-ITER's. This discrepancy grows with $\mathcal{A}$ increasing towards unity (grey arrow in the plot), thus being particularly significant for like-particle interactions (here, $\mathrm{Ne}^{z+}/\mathrm{Ne}^{w+}$ with $z \neq w$), and for low $\mathcal{N}$. On the other hand, for a given n_e, the magnitude of the friction force tends to zero for low enough $\mathcal{N}$ (i.e. substantial disparity in the density of interacting species): in fact, $|S^{\mathrm{m}}_{ba,\mathrm{fr}}| \propto n_a n_b = \mathcal{N} \cdot [\max\{n_a; n_b\}]^2 \leqslant \mathcal{N} \cdot n_\mathrm{e}^2 \; \forall a, b \in \mathcal{S}^+$, at least in SOLPS-ITER's equation (2).

Overall, the ultimate impact on the momentum balance solution is unclear. The consequences of incongruities in the friction force formulations should mostly affect the physics in the proximity of the divertor targets, where both $V_{a\parallel}$ and $|\partial_x V_{a\parallel}|$ are large [48]. This is therefore of potential concern.

The above exemplifying argument has been successfully condensed in a simple analytical form and pictorially illustrated. Unfortunately, the same is instead not possible neither for the electron–ion friction force (only its collision time can be assessed, as per equation (13), and suggests how differences might exist at large), nor for the thermal force (equations (2) and (4)). These are therefore not further commented on in the present work, though deserving dedicated investigations.

Similarly, implications of (and reasons behind) the different formulations are not analysed here, but would be worthwhile addressing, likewise comparing SOLPS-ITER and SOLEDGE2D Zhdanov formulations, and SOLEDGE2D with η^{CL}_{ax}-dependent terms. Figure 12 indeed depicts the relative importance of $\eta^{\mathrm{CL}}_{ax}\partial_x V_{a\parallel}$ in SOLPS-ITER momentum equations (normalised to $|m_a n_a V_{a\parallel}(b_x V_{a\parallel} + V^{\mathrm{diff}}_{ax,n} + V^{\mathrm{corr}}_{ax})| + |(\eta^{\mathrm{CL}}_{ax} + \eta^{\mathrm{AN}}_{a})\partial_x V_{a\parallel}| + |\eta^{\mathrm{CL}}_{ax} V_{a\parallel}\partial_x \ln h_z|$): the absence of these terms in SOLEDGE2D could be playing a major role in the present work—and could have in [18] too.

5.2.3.2. *Simplified momentum equation in UEDGE.*

Upon slight manipulation, the simplified equation (6) can be reformulated as: $\partial_t(m_z V_{z\parallel}) \sim m_z V_{z\parallel}/\tau^{\mathrm{UE}}_{\mathrm{pz}} = f(V_{\mathrm{D}^+\parallel})$, where the function $f(V_{\mathrm{D}^+\parallel})$ evidently encapsulates the contribution of pressure, friction, and thermal forces.

Omitting impurity inertial effects to retrieve equation (6) is legitimate whenever parallel velocities are much smaller than the sonic speed away from the divertor plates [20]. This assumption is found to be appropriate for UEDGE neon ionisation stages only in the near SOL (not shown for reasons of space), while the impurity flow speeds approach sonic conditions elsewhere in the divertor volume up to the X-point (also confirmed by SOLPS-ITER).

The impact of this simplification on the solution is unclear, but would be worthwhile investigating by utilising the full impurity momentum equations in UEDGE.

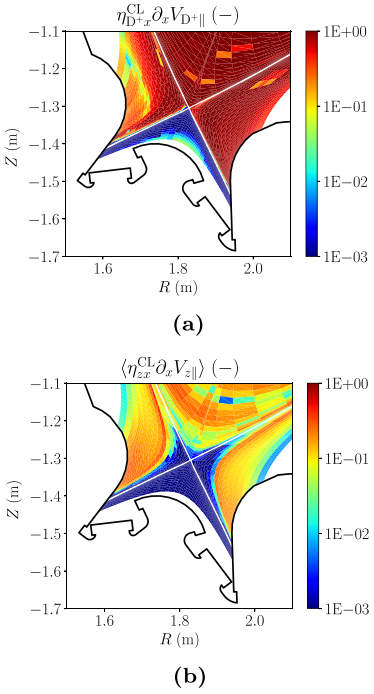


Figure 12. Relative importance of SOLPS-ITER terms involving the classical parallel viscosity for deuterium (*a*) and averaged over neon ionisation stages (*b*), both unaccounted for by SOLEDGE2D.

5.3. *Investigating observed differences in code results*

In this section, we consider some of the discrepancies in the code predictions. By dissection of the solution and the physics/geometry models, an interpretation of some of the phenomena observed is attempted.

5.3.1. *Penetration of puffed neutral deuterium at OMP.*

5.3.1.1. *Over-penetration in UEDGE.*

As in [18], the suitability of UEDGE solving equation (11) for a unified temperature between ions $\mathcal{S}^+$ and the fluid-neutral species $\mathcal{S}^0 = \{\mathrm{D}\,;\,\mathrm{Ne}\}$ (i.e. $T_\mathrm{D}/T_\mathrm{i} = T_\mathrm{Ne}/T_\mathrm{i} = 1$, section 2.1.5) is assessed.

Figures 13(*a*) and (*b*) show $T_\mathrm{D}/T_\mathrm{i}$ and $T_\mathrm{Ne}/T_\mathrm{i}$, respectively, in SOLPS-ITER. Spatial-average values[20] of $T_\mathrm{D}/T_\mathrm{i} = 1.10$ and $T_\mathrm{Ne}/T_\mathrm{i} = 1.58$ are obtained throughout the domain. Both cases substantially depart from unity: (i) approaching 10 along the divertor legs, resulting from the high-energy tail of the atom energy distribution [18], scarcely-populated and therefore not of particular concern; (ii) approaching 0.1 in the far SOL, as also suggested by [31], and at the OMP, as in [18].

At the very OMP, electron and D^+ main ion density in UEDGE are markedly over-estimated in the core, by up to 2.45 and 3.63, respectively, compared to the other codes (section 4.1). An enhanced core fuelling was already observed in section 5.3 of [18], albeit to a lower extent: the

[20] With cell-specific weights dictated by the amount of neutral particles therein, normalised to the total amount of neutrals in the entire domain.

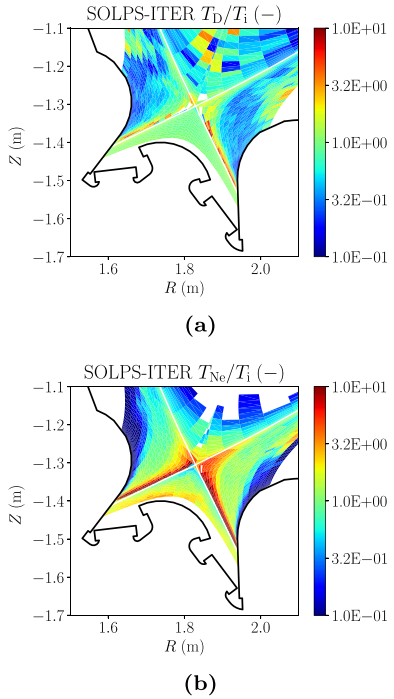


Figure 13. Temperature ratio between neutral deuterium and ions (*a*), and between neutral neon and ions (*b*) in SOLPS-ITER.

driving cause was identified in the UEDGE assumption of $T_D = T_i$.

Although appropriate in the divertor volume (as here, figure 13), assuming $T_D/T_i = 1$ results in puffing the D gas in UEDGE at the unrealistically high temperature of $T_D^{puff} = T_i = 201$ eV (83 eV in [18]). Conversely, $T_D/T_i \sim 0.15$ (as in [18]) and $T_D = 27$ eV in the OMP far SOL for SOLPS-ITER. The consequence of the $T_D/T_i = 1$ assumption should therefore be more significant here than in [18], implying even longer neutral mean-free-paths and stronger over-penetration of neutrals into the core region in UEDGE. And this is indeed found to be the case: neutral deuterium atoms crossing the separatrix in UEDGE are found to be $8.40 \cdot 10^{21}\,\mathrm{D}\cdot\mathrm{s}^{-1}$, compared to $3.36 \cdot 10^{21}\,\mathrm{D}\cdot\mathrm{s}^{-1}$ in SOLPS-ITER, a factor 2.5 greater (only 1.5 in [18]).

Corroborating evidence of the over-penetration is further found in the UEDGE solution.

With constant D^{AN}, the non-linear shape of the core plasma density profiles (figures 2(*a*) and (*e*)) is symptomatic of the presence of a significant volumetric particle source of electrons and main ions.

The over-penetration also explains (in-part at least) differences in the OMP temperature profiles in UEDGE (figures 2(*b*) and (*f*)): a factor 1.40 (1.48) lower for T_e and 1.86 (3.50) for T_i compared to SOLPS-ITER (SOLEDGE2D). Figure 14 illustrates this effect via plots of the different components of the poloidally-integrated radial power fluxes computed by SOLPS-ITER and UEDGE. The presence of an extra particle source in the core requires exhausting an enhanced radial particle flux, which drives higher radial convective power fluxes in UEDGE compared to SOLPS-ITER (dash-dotted lines). Owing to the common P_{in}, this higher convective flux brings along a reduction in the radial conductive flux (dashed lines), and consequently a reduction in the T_i gradients. Lower temperatures in the core region of UEDGE follow.

UEDGE also predicts a neutral D total heat flux orders of magnitude larger than SOLPS-ITER's (dotted line bottoming the graph) all throughout the OMP, indicating a considerable neutral flux into the closed field line region.

The above compellingly supports the hypothesis of the over-penetration due to $T_D = T_i$, significantly worse at higher exhaust powers/upstream temperatures, compared to [18]. Repeating the exercise performed in [18] of reducing the T_D/T_i ratio in UEDGE for a direct proof is therefore not attempted in this work. Additional consequences of the above are detailed in section 5.3.4.2.

Finally, with the UEDGE over-penetration enhancing core fuelling (with corresponding decrease in SOL fuelling) and the radial particle flux, steep density gradients develop across the separatrix in UEDGE and extend into the SOL, resulting in lower densities in this region: up to a 6- and 11-fold drop in n_e and n_{D^+}, and up to a 2.5- and 3-fold increase in T_e and T_i in the far SOL, respectively.

5.3.1.2. Mesh-boundary artefact in SOLPS-ITER. Both SOLPS-ITER and SOLEDGE2D feature a non-monotonic profile of n_{D^+} in the OMP SOL. The underlying cause is related to the D_2 puffing in the region, which results in a localised significant ionisation source of $\mathcal{S}^0$ deuterogenic species, absent in the colder SOL of [18] where the D_2 puff strength was also a factor 2 smaller.

Figure 15(top) details the normalised profiles of the dominant reactions[21] involving deuterogenic neutral species in SOLPS-ITER, compared to the normalised n_{D^+}: D_2 preferentially undergoes electron-ionisation (EI) in the far SOL to give D_2^+ which, in turn, dissociates (DS) to D^+ and D, the former enhancing n_{D^+} in the very far SOL, and the latter further penetrating inwards before electro-ionisation.

In SOLPS-ITER, a continuous rise in n_{D^+} in the far SOL is so produced, which qualitatively differs from SOLEDGE2D's (figure 15, bottom), where a local maximum is followed by a constant decrease up to the wall. The strong peaking of D_2-EI and D_2^+-DS, with corresponding lower penetration, observed in SOLPS-ITER is a spurious effect associated to the presence of the artificial boundary (red line in figure 1 and in figure 15, similarly to section 5.6 of [18, 49]). Such feature indeed persists even when the SOLEDGE2D reaction set is adopted in SOLPS-ITER (section 5.3.5.2).

5.3.2. Double-peak feature in the heat flux at the inner target. Both SOLEDGE2D and UEDGE present peculiar doubly-peaking heat flux profiles (figure 3(*g*)) at the inner target, which neither currents nor drifts are responsible for, being de-activated in the present work (section 2).

[21] `AMJUEL H.4 2.2.9, AMJUEL H.4 2.2.12, AMJUEL H.4 2.1.5`, respectively.

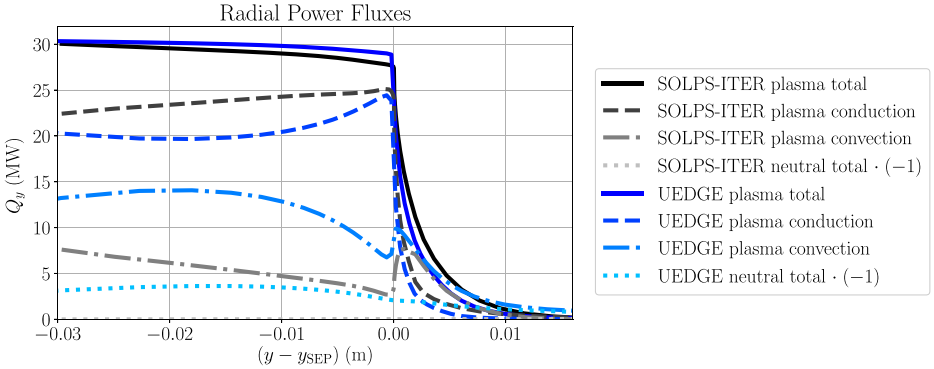


Figure 14. Break-down of outer mid-plane radial power fluxes in SOLPS-ITER (shades of grey) and UEDGE (shades of blue). Positive values identify fluxes along the $+y$ direction (core to edge), viceversa for negative figures (rendered as positive).

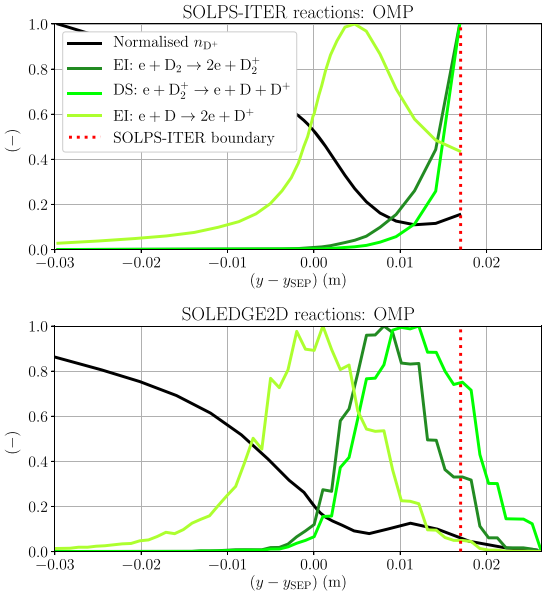


Figure 15. Break-down of major deuterogenic reaction rates (shades of green, normalised) at outer mid-plane for SOLPS-ITER (top) and SOLEDGE2D (bottom). The resulting main-ion density (black, normalised) and SOLPS-ITER's artificial radial boundary (red) are also shown.

5.3.2.1. Double peak in UEDGE. Figure 16 shows a reconstruction of the perpendicular heat flux in UEDGE, obtained by approximately accounting for the additional contribution $\tilde{q}_\perp^{\text{rad}}$ that would have been provided by the plasma convection/-conduction, had it not been radiated. In particular, $\tilde{q}_\perp^{\text{rad}}$ is computed for each radial (y) cell along the target by integrating $S_{\text{tot}}^{\text{rad}}$ (figure 6) along the poloidal (x) direction, from the target up to the X-point:

$$\tilde{q}_\perp^{\text{rad}}(y_j) = \frac{1}{\sigma_\perp(y_j)} \sum_{i=i_T}^{i_X} S_{\text{tot}}^{\text{rad}}(x_i, y_j)\, V(x_i, y_j) \qquad (17)$$

where i and j are respectively the x and y cell indices, the sum runs from the target poloidal position i_T to the X-point location i_X, $\sigma_\perp$ is the projected area, and V the cell volume.

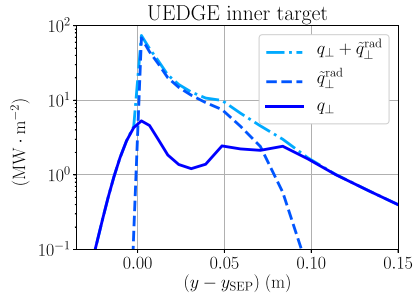


Figure 16. Reconstruction of inner target heat flux for UEDGE. The term $\tilde{q}_\perp^{\text{rad}}$ represents the portion of heat flux the target would have approximately received, had it not been radiated (details in section 5.3.2.1).

Equation (17) does not account for cross-field diffusion, and different flux tubes are independently considered.

The resulting reconstructed heat flux $(q_\perp + \tilde{q}_\perp^{\text{rad}})$ in figure 16 suggests that the existence of the double peak in UEDGE could be entirely appointed to the volumetric heat sink from radiation. This heat sink is indeed predominantly localised in the flux tubes where high electron density and proper temperature promote strong radiation emission. In the current semi-detached scenario, the position of the minimum $q_\perp$ correlates with the onset of plasma reattachment in the far SOL, where T_e rises above the sub-eV level (inset of figure 3(b)).

Worthwhile stressing is the persistence of the double peak even when further adding the actual radiative heat load to the perpendicular heat flux, as computed via the UEDGE inner tool[22]. This therefore supports the analyses above.

The primary conclusion of this inner target analysis is to caution on the interpretation of double-peak heat flux profiles, potentially arising from potent volumetric power losses, hence unrelated to the known effect of drifts [52] and resonant magnetic perturbation (RMP) fields [53, 54].

[22] Although a 3D radiative heat load computation [50, 51] would be more accurate, this would only quantitatively, not qualitatively, impact the conclusions in the present paragraph.

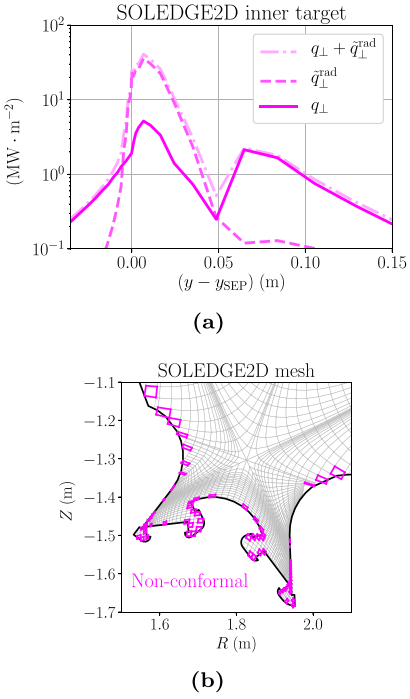


Figure 17. (*a*) Approximate reconstruction of inner target heat flux for SOLEDGE2D (details in section 5.3.2.1). (*b*) SOLEDGE2D mesh in grey: representative non-conformal cells (not wall-aligned) in magenta; cells with more than one vertex outside the chamber (black) not shown for the sake of clarity—blank regions within the chamber being a spurious consequence of this illustrative example.

5.3.2.2. Double peak in SOLEDGE2D. The double peak featured at the inner target by SOLEDGE2D (figure 17(*a*)) does not entirely disappear when accounting for the radiation losses via equation (17). This is in-part attributed to the structure of boundary mesh cells in SOLEDGE2D, which does not necessarily conform to the wall in the far SOL (magenta in figure 17(*b*), also visible in figure 1 of [55]).

Despite still field-aligned, non-conformal boundary cells at the target are poloidally orthogonal to the magnetic flux surface, hence providing no poloidal-tilting reduction to any perpendicular flux—hence the over-estimation of $q_\perp$ and second peak.

In this instance, non-conformal cells appear from $(y - y_{\mathrm{SEP}}) \sim 7$ cm onwards along the inner target SOL in SOLEDGE2D (and similarly for the step-like structures visible in the inset of). The heat flux in figure 3(*h*) and the neutral neon density in figure 4(*e*) also show reminiscences of this effect in the far SOL of the outer and inner target, respectively, with evident step-like patterns.

Considering the present SOLEDGE2D solution in its entirety, such mesh non-conformity should not give any noticeable concern. The same conclusion would not necessarily apply if sputtering was considered, with the over-estimation of particle fluxes where the plasma reattaches in the far SOL [40].

5.3.3. Degree of detachment at the outer target. The outer target heat flux of SOLPS-ITER does quantitatively and qualitatively resemble its inner counterpart, without featuring a double peak (figures 3(*d*) and (*h*)). SOLEDGE2D and UEDGE also show an Eich-like heat flux profile at the outer target, but peaking a factor 2.0 above and 2.5 below SOLPS-ITER's, respectively.

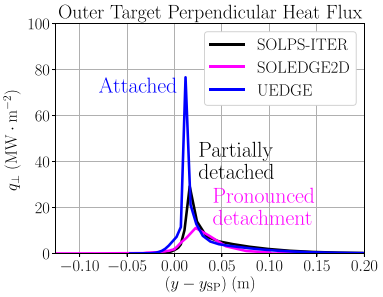


Figure 18. Outer target heat flux for the three codes, precisely following the varying degree of detachment of which in [56], and labelled accordingly.

Figure 18 pictures the outer target $q_\perp$ profiles, remarkably similar to the behaviour of the heat flux as a function of the detachment degree shown in [56]. The difference in $q_\perp$ magnitude and shape can therefore be attributed to differing degree of detachment achieved in this location by each code. This conclusion is also supported by the fact that, at the outer target, $(q_\perp + \tilde{q}_\perp^{\mathrm{rad}})$ from equation (17) is matched by UEDGE and SOLPS-ITER within a much more satisfactory 35%.

5.3.4. Density flooring and effective charge distribution.

5.3.4.1. Density flooring of impurity species. A notable feature observed in this study is the non-negligible impact of the 'density flooring': this is a user-defined minimum allowed density per ion species in the domain, intended to prevent the density from dropping to near-zero values, potentially causing numerical instabilities. This floor is maintained by an artificial source in the affected grid cells, and it is employed by all the three codes. UEDGE, being the fastest code, was used to explore this effect.

Particle fluxes across the separatrix (SEP) are analysed for both D and Ne species. Table 2 shows the break-down of neutral and ion fluxes across both core and SEP in UEDGE. At the core boundary, the net fluxes of ions and neutrals are consistent with the core boundary conditions specified in this setup ($5 \cdot 10^{20}\,\mathrm{s}^{-1}$ for D, zero flux for Ne—section 3). However, at the separatrix, whilst the net outward flux for D is consistent ($5 \cdot 10^{20}\,\mathrm{s}^{-1}$ again), Ne presents a sizeable disparity, with an outward net flux of $\sim 4 \cdot 10^{17}\,\mathrm{s}^{-1}$ (table 2, red)—in spite of the core boundary showing zero net Ne flux, and the only Ne source in the domain being from the PFR puffing ($6 \cdot 10^{19}\,\mathrm{Ne}\cdot\mathrm{s}^{-1}$ in UEDGE). This is non-negligible in comparison to the Ne transport in/out of the core region itself, suggesting the presence of a significant particle imbalance in this domain, despite the successful convergence of the code solution.

The density floor of the impurity ions ($10^{10}\,\mathrm{m}^{-3}$, typical in UEDGE) is determined to be responsible for this imbalance. Through most cells in the core region, the low charge states

Table 2. Break-down of UEDGE ion and neutral cumulative radial fluxes across the core and separatrix (SEP), for the baseline case with density floor of $10^{10}\,\mathrm{m}^{-3}$, and the newly explored case (*) with density floor of $10^{8}\,\mathrm{m}^{-3}$. Positive values identify fluxes along the $+y$ direction (core to edge), and viceversa. Neon imbalance being non-negligible (negligible) compared to neon puffing of $6\cdot10^{19}\,\mathrm{Ne}\cdot\mathrm{s}^{-1}$ in red (blue).

Region	CORE (s^{-1})		SEP (s^{-1})		SEP* (s^{-1})	
Species	D	Ne	D	Ne	D	Ne
Neutrals	$+6.26\cdot10^{6}$	$+1.45\cdot10^{2}$	$-8.40\cdot10^{21}$	$-1.01\cdot10^{18}$	$-8.41\cdot10^{21}$	$-8.94\cdot10^{17}$
Ions	$+4.99\cdot10^{20}$	$+1.67\cdot10^{5}$	$+8.90\cdot10^{21}$	$+1.40\cdot10^{18}$	$+8.91\cdot10^{20}$	$+8.98\cdot10^{17}$
Total	$+4.99\cdot10^{20}$	$+1.67\cdot10^{5}$	$+4.99\cdot10^{20}$	$\mathbf{+3.85\cdot10^{17}}$	$+4.99\cdot10^{20}$	$\mathbf{+3.76\cdot10^{15}}$

of neon engage the floor value, consistently with a high ionisation sink at high temperatures. This results in an artificial net production rate of $3.84\cdot10^{17}\,\mathrm{s}^{-1}$ from volumetric sources, equivalent to the particle imbalance found from fluxes across the separatrix (table 2, red). Extending the artificial impurity particle source evaluation to the full mesh domain, the total additional particle source approaches ∼1% of the total Ne puff magnitude. When the impurity density floor in UEDGE is reduced to $10^{8}\,\mathrm{m}^{-3}$ (*), the particle imbalance decreases in-kind by two orders of magnitude to $3.76\cdot10^{15}\,\mathrm{s}^{-1}$ inside the separatrix (table 2, blue), confirming the density floor as the root cause. This numerical phenomenon is however not limited to UEDGE, and affects the other two codes to a certain extent.

The SOLEDGE2D solution hits its density floor of $10^{13}\,\mathrm{m}^{-3}$ in the red areas of figure 19(*a*) with Ne^{3+}, representative of all stages up to Ne^{6+} in the core. The artificial production of low-medium neon ionisation stages in the SOLEDGE2D core could be sizeable, given the already noticeable effect the UEDGE floor, three orders of magnitude lower than SOLEDGE2D's, had.

This same argument equally holds for high charge states in the far SOL which, in SOLEDGE2D, engage the density floor in the close proximity of the wall in the extended plasma mesh (red in figure 19(*b*) for Ne^{10+}, representative of all the stages down to Ne^{7+}). Hence, the $Z_{\mathrm{eff}}\sim7.0$ there localised (yellow in figure 19(*d*) and around the pump ducts in figure 5(*b*)) is ascribed to this numerical artefact of SOLEDGE2D.

In SOLPS-ITER simulations, the neon density floor is set to $10^{8}\,\mathrm{m}^{-3}$. Although the artificial particle generation is negligible in UEDGE at this level, a small imbalance is observed in SOLPS-ITER neon fluxes across the separatrix.

Deleterious per se, the particle imbalance and additional impurity throughput, generated by the artificial density floor, could have further significant consequences (section 5.3.6). Crucially, this effect would be worse for higher-Z impurities, with additional charge states providing extra potential for artificial particle generation. Therefore, the impurity density floor is to be set appropriately low to avoid malicious consequences.

5.3.4.2. Z_{eff} in UEDGE. The predicted Z_{eff} prominently varies from code to code, as evidenced by the rendering of figure 20 in computational space. In SOLPS-ITER and SOLEDGE2D, Z_{eff} takes relatively high values through the far SOL and core regions, often at $Z_{\mathrm{eff}}>4$ and peaking at $Z_{\mathrm{eff}}\sim7$ and ~9 for SOLPS-ITER and SOLEDGE2D, respectively.

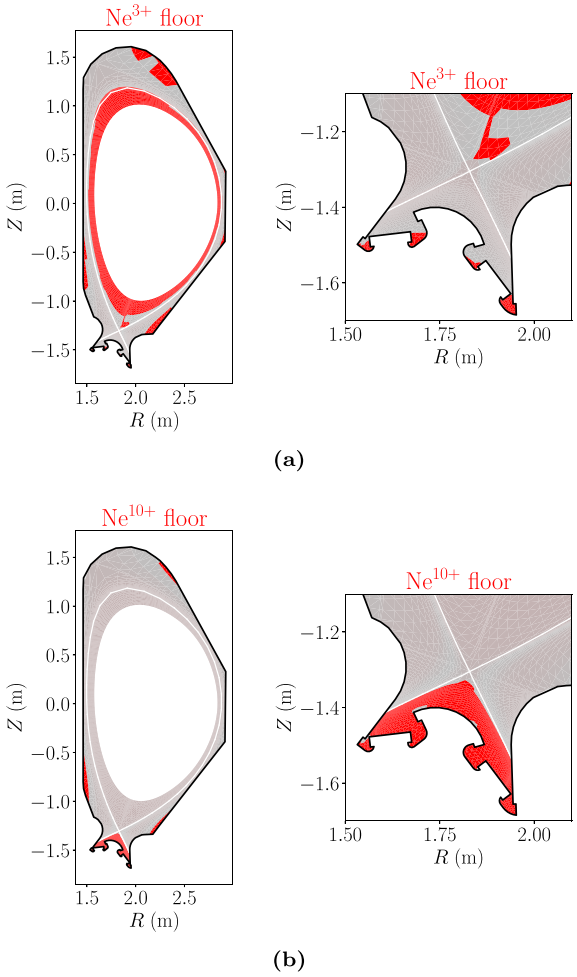


Figure 19. SOLEDGE2D logical maps of Ne^{3+} (*a*) and Ne^{10+} (*b*), with the artificial density floor ($10^{13}\,\mathrm{m}^{-3}$) active where red, inactive where grey.

The D_2 puffing at 0.03 eV in EIRENE at OMP contributes to a strong volumetric D^{+} source in the OMP far SOL (section 5.3.1.2), forcing Z_{eff} to decrease towards unity in this deuterium-dominated zone. This effect is illustrated in figure 20(*a*) (top) for SOLPS-ITER, at the upper end of the white vertical dotted line, and in figure 20(*b*) for SOLEDGE2D—this feature goes missing

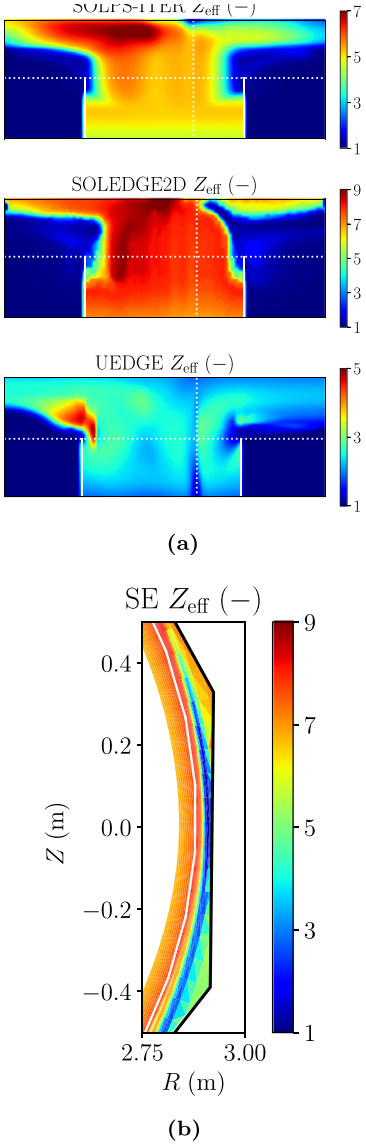


Figure 20. (a) Effective charge distribution $Z_{\rm eff}$ in the computational domain of SOLPS-ITER (top), SOLEDGE2D interpolated onto SOLPS-ITER grid (centre), UEDGE (bottom), with ad hoc colourbar limits. (b) SOLEDGE2D (SE) $Z_{\rm eff}$ distribution in real space around the OMP, featuring a drop towards unity missed when interpolated onto SOLPS-ITER radially-limited computational grid (figure 20(a), centre).

when the SOLEDGE2D solution is interpolated onto the radially-limited SOLPS-ITER computational grid to produce figure 20(a) (centre).

On the other hand, UEDGE features a much smaller $Z_{\rm eff} < 5$ (figure 20(a), bottom). This results from the over-penetration of puffed deuterium in UEDGE (section 5.3.1.1): the deuterium volumetric source and the corresponding deuterium-dominated zone ($Z_{\rm eff} \sim 1$) shift more deeply in the core plasma (around the lower end of the white vertical dotted line of the OMP), impairing the production of high neon ionisation stages by leading to higher main ion densities and lower temperatures in the core.

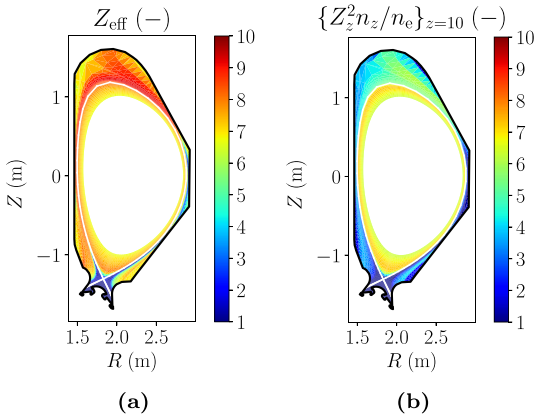


Figure 21. SOLEDGE2D overall $Z_{\rm eff}$ (a) and standalone contribution to $Z_{\rm eff}$ of Ne^{10+} ($z = 10$) (b).

5.3.4.3. $Z_{\rm eff}$ in SOLEDGE2D. SOLEDGE2D produces a distinctive feature, as pictured by figure 21(a): $Z_{\rm eff} > 8$ all throughout the top of the chamber, included by the extended plasma mesh. Responsible of this feature are Ne^{8+}, Ne^{9+} and Ne^{10+} (figure 21(b) for the latter), respectively accounting for ~ 1, ~ 1, and ~ 6 in such region. This is likely unrelated to the density floor (section 5.3.4.1), as suggested by figure 19(b), representative of all the three species.

Despite the potential for electronic RC in this relatively cold plasma ($5\,{\rm eV} \leqslant T_{\rm e} \leqslant 75\,{\rm eV}$), and an insignificant ionisation source (ionisation energies 239 eV, 1196 eV and 1362 eV, respectively), a surplus of Ne^{8+}, Ne^{9+} and Ne^{10+} could be supplied by potent radial transport outward the core plasma ($\partial_y n_z < 0$). This could be the case in the present scenario, where not any neoclassical inward-pointing impurity pinch velocity [25, 57] is modelled. Ancillary SOLPS-ITER investigations (not shown) tentatively indicate that the $Z_{\rm eff}$ spatial distribution could be significantly altered by suppressing $D^{\rm AN}$ for the only neon high ionisation stages, simplistically mimicking the effect of an inward pinch. Additionally, sections 16.2 and 16.4.7 of [27] report how low friction experienced by the fluid flow, e.g in low plasma density regions, would not allow for enough time for volumetric recombination to occur in the first place. This might be particularly the case in SOLEDGE2D, with a smaller friction force than SOLPS-ITER (section 5.2.3.1).

Overall, how physically genuine such impurity presence at the top of the chamber is remains dubious. Non-trivial activity around the secondary X-point in single null magnetic topologies is in fact expected [15, 58], at least in terms of plasma heat load. The impurity accumulation observed in our SOLEDGE2D solution, and corresponding concern for wall erosion, might be one additional item to be accounted for.

5.3.4.4. $Z_{\rm eff}$ in SOLPS-ITER. As pictured in figure 2, throughout the core region SOLPS-ITER simultaneously features a lower $Z_{\rm eff}$, higher $n_{\rm D^+}$, and lower $T_{\rm i}$ relative to SOLEDGE2D. Even without here delving in its primary cause (section 5.3.5.2), the present heuristically shows how a lower

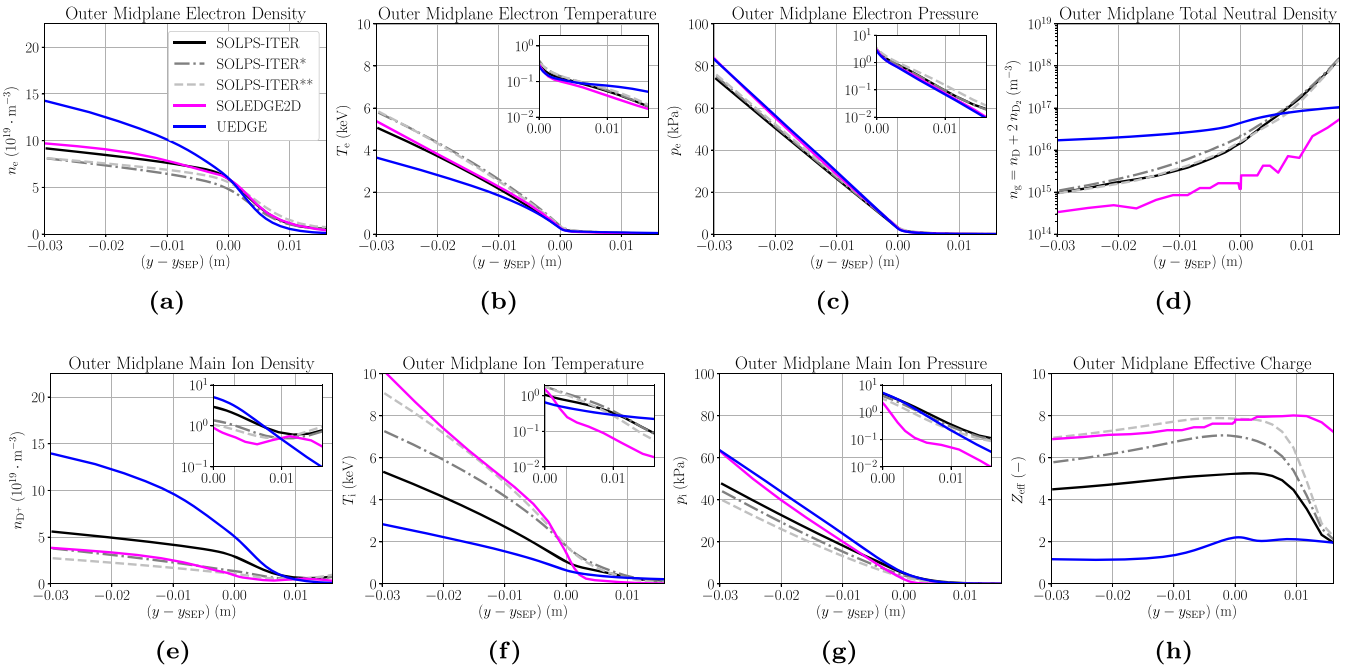


Figure 22. Plasma and neutral profiles at outer mid-plane (separatrix at $y - y_{\mathrm{SEP}} = 0$). The insets show the profiles in logarithmic scale. Black solid line = baseline SOLPS-ITER simulation (section 4), with default set of reactions and puff rate of $4 \cdot 10^{19}\,\mathrm{Ne} \cdot \mathrm{s}^{-1}$. Dark grey dash-dotted line (SOLPS-ITER*) = SOLPS-ITER simulation without neutral-neutral collisions and $1 \cdot 10^{20}\,\mathrm{Ne} \cdot \mathrm{s}^{-1}$. Light grey dashed line (SOLPS-ITER**) = SOLPS-ITER* simulation with SOLEDGE2D set of reactions.

Z_{eff} alone is sufficient to subsequently produce higher n_{D^+} and lower T_{i} (viceversa for a higher Z_{eff}).

SOLPS-ITER and SOLEDGE2D show an excellent agreement for the electron profile at OMP (figure 2(*a*)). To maintain quasi-neutrality to a common n_{e}, lower Z_{eff} implies higher n_{D^+}. Therefore, SOLPS-ITER's smaller Z_{eff} leads to an enhanced n_{D^+}, which is expected.

However, despite the high Z_{eff} of the scenario, the concentration of the main ion (exceeding 80% in the two codes) dominates the overall ion pressure, and $n_{\mathrm{i}} T_{\mathrm{i}} \sim n_{\mathrm{D}^+} T_{\mathrm{i}}$. Hence, given the same input power in the two codes (section 3.2.1) , the enhanced n_{D^+} implies a lower T_{i} in SOLPS-ITER from ion energy balance.

This argument could also justify the varying y-gradient in T_{i} of SOLEDGE2D despite the constant transport coefficients (section 4): the T_{i} profile is affected by Z_{eff} and n_{D^+} which vary along y.

These results should be sufficient evidence for the reader to be cautious on the vicious chain of effects a mismatch in Z_{eff} could lead to. This issue would be exacerbated by the uncertainty affecting the impurity anomalous transport (section 5.3.4.3). Solving for different species-specific ion temperatures should ameliorate matters, at least in this respect, by breaking the link between n_{D^+} and T_{i}.

5.3.5. Atomic and molecular reactions.

5.3.5.1. STRAHL rates in UEDGE. Coherently with [59], a 5% increase in total radiated power and 16% decrease in $n_{\mathrm{e}}^{\mathrm{SEP}}$ result from running SOLPS-ITER with the STRAHL-based rate coefficients used in UEDGE, instead of the ADAS default (section 2.1.1). Not accompanied by any further noteworthy differences, this is discarded as a leading source of disparities in UEDGE compared to SOLPS-ITER and SOLEDGE2D.

5.3.5.2. EIRENE reactions in SOLPS-ITER and SOLEDGE2D. Figure 22 compares the baseline results of the three codes to: a SOLPS-ITER simulation without neutral-neutral collisions (SOLPS-ITER*); the SOLPS-ITER* simulation also with SOLEDGE2D reduced set of reactions of table 1 in [18] (SOLPS-ITER**). In these two new cases the neon puffing can be increased to $1 \cdot 10^{20}\,\mathrm{Ne} \cdot \mathrm{s}^{-1}$ without failing convergence, hence matching SOLEDGE2D. This allows P_{rad} to reach 20.2 MW and 22.2 MW in SOLPS-ITER* and SOLPS-ITER**, respectively, thus within 2% and 8% of SOLEDGE2D's 20.5 MW.

A dramatic qualitative and quantitative reconciliation with SOLEDGE2D is apparent in the OMP core for Z_{eff}, n_{D^+} and T_{i}, consistently with section 5.3.4.4. However, no improvement is observed neither for n_{D^+} (far SOL) nor for T_{i} (near and far SOL). For the former, this is ascribed to effects related to the SOLPS-ITER limited mesh extension (section 5.3.1.2), while, for the latter, it remains unclear (but potentially related to SOLEDGE2D's high Z_{eff} in the far SOL—section 5.3.4.3).

The remaining quantities, in addition to those of figure 23, similarly suggest that not all the discrepancies are ameliorated, with some actually being exacerbated instead.

The degree of agreement in the plasma volume at large also varies on a case-to-case basis. Employing SOLEDGE2D reactions in SOLPS-ITER in [18] saw a considerable qualitative and quantitative improvement in neutral density distributions

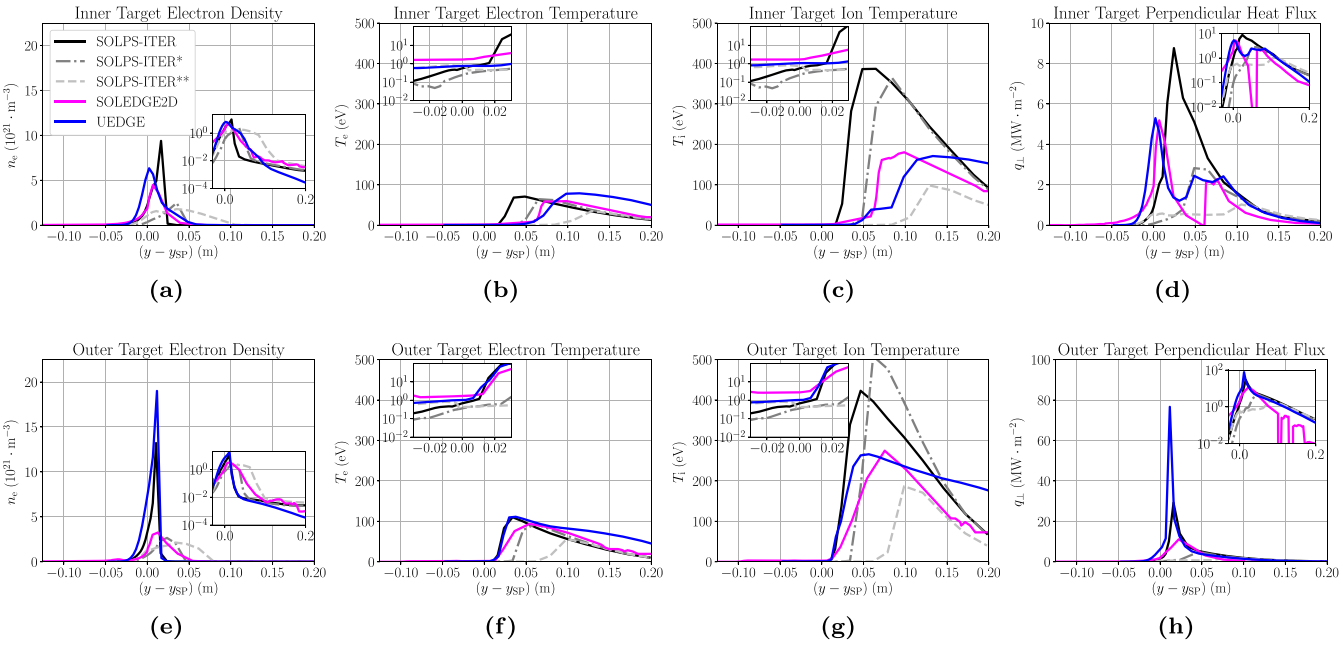


Figure 23. Plasma profiles at the inner and outer divertor targets (strike point at $y - y_{SP} = 0$). Perpendicular heat fluxes with different vertical axis to improve readability. The insets show the profiles in logarithmic scale.

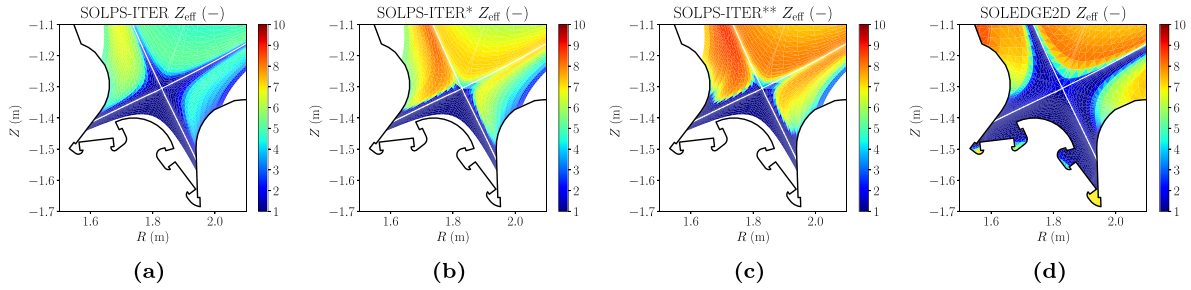


Figure 24. Effective charge Z_{eff} distribution in the divertor for: (*a*) SOLPS-ITER baseline simulation (section 4), with default set of reactions and puff rate of $4 \cdot 10^{19}\,\mathrm{Ne} \cdot \mathrm{s}^{-1}$; (*b*) SOLPS-ITER simulation without neutral-neutral collisions and $1 \cdot 10^{20}\,,\mathrm{Ne} \cdot \mathrm{s}^{-1}$ (SOLPS-ITER*); (*c*) SOLPS-ITER* simulation with SOLEDGE2D set of reactions (SOLPS-ITER**); (*c*) SOLEDGE2D.

in the PFR, however absent in the present case (not shown for reasons of space). Nonetheless, SOLPS-ITER's spurious gradients atop of the artificial PFR boundary vanish, as per [18]. A notably better match of Z_{eff} is observed in figure 24 all throughout the SOL and core volumes.

To draw conclusions from this, some differences existing among SOLPS-ITER and SOLEDGE2D follow from SOLPS-ITER failing to reach the same neon puffing rate and total radiated power of SOLEDGE2D. On the one hand, the present paragraph highlights the reduced atomic-molecular reaction set of SOLEDGE2D to be the driver behind this factor. On the other hand, the improved agreement follows from the simplification of the physics models in SOLPS-ITER, therefore unsatisfactory overall. Also worthwhile noting is the impact neutral-neutral collisions alone have had in this context.

5.3.6. Radiation emission distribution. SOLEDGE2D radiation emission distribution in figure 25(computational space) is seen to wildly differ from SOLPS-ITER's and UEDGE's, as also supported by the integral radiated power per plasma region (figure 26).

Coherently with its reduced heat flux at the outer target (figure 3(*h*)), SOLEDGE2D presents a marked re-allotting of radiated power from the downstream outer divertor (OUT-DIV) towards the upstream SOL and core. According to figure 26, the different SOLEDGE2D reactions cannot be held responsible, for not even SOLPS-ITER** (section 5.3.5.2) can reproduce this feature. Instead, the density-floored neon low-medium ionisation stages in the core of SOLEDGE2D (section 5.3.4.1) do offer a spurious surplus of radiating species. Although this helps explaining part of the discrepancy, unfortunately, the lack of a species-wise break-down of the radiation/particle sources and fluxes impairs any further insights.

On a different note, an additional observation from figure 25 provides additional evidence for the puffed gas over-penetration in UEDGE (section 5.3.1.1), with a deuterium-driven emission peak in the OMP core plasma (lower end of the white vertical dotted line in figure 25, bottom), instead

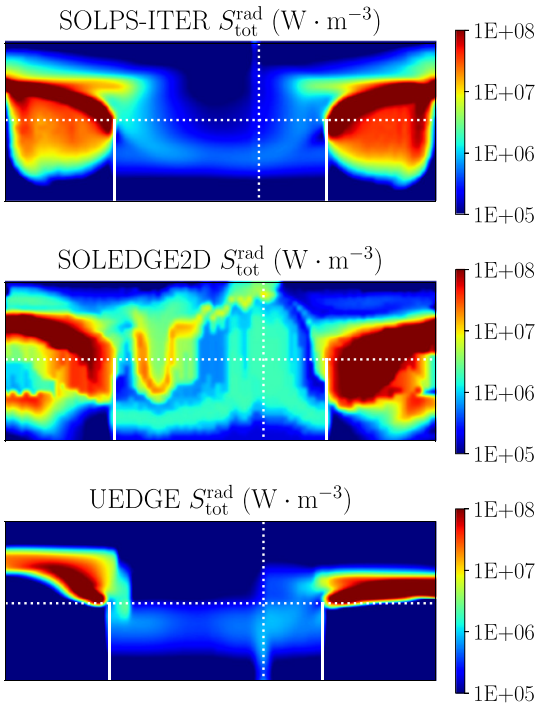


Figure 25. Radiation emission distribution in the computational domains of SOLPS-ITER (top), SOLEDGE2D re-interpolated on SOLPS-ITER grid (centre), and UEDGE (bottom).

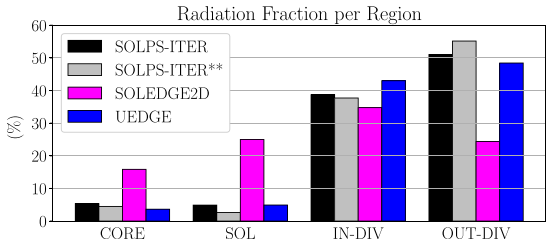


Figure 26. Radiation fraction per region of plasma. Radiation fraction = proportion of radiation emitted in a certain region, normalised to the total. Regions: CORE = core plasma; SOL = edge plasma above the X-point; IN-DIV (OUT-DIV) = inner (outer) divertor comprising inner (outer) SOL and inner (outer) PFR below the X-point.

apparent in the far SOL in SOLPS-ITER (upper end of the white vertical dotted line in figure 25, top), and consistent with section 5.3.4.2.

5.3.7. Neutral neon. An unusual feature affects the neighbourhood of the PFR boundary in SOLPS-ITER's figure 13, where $T_{\mathrm{Ne}}/T_{\mathrm{i}} > 1$, despite neon being puffed at 0.03 eV and $T_{\mathrm{i}} \sim 0.1$ eV in that region. This is currently unexplained, although tentatively posited to be due to one among (or a combination of): (i) the artificial nature of such boundary in SOLPS-ITER; (ii) any residual energy retained by the neon when recombining from Ne^{1+} (section 2.2); (iii) the invalidity of the ADAS-based reaction rate for temperature below 0.2 eV [22].

In UEDGE's result, with neon being puffed in the cold sub-eV PFR, no over-penetration issue such as in section 5.3.1.1 is observed. UEDGE's neutral neon density distribution (figure 4(*f*)) is however striking compared to SOLPS-ITER's and SOLEDGE2D's—with very high density present in the immediate proximity of the pumping surfaces. Whether this is a geometrical effect of compression in the tilted target plate regions, or a particle-balance effect related to the pumping surfaces and the flux required to be removed there, is unclear. This may nonetheless have a significant impact on the solution, and could be related to (or be) the cause of the higher level of detachment on the inner leg in UEDGE.

6. Conclusions

Building on the cross-code comparison of Moscheni *et al* (2022) [18] for a low-power pure-deuterium scenario, the present work performs a similar assessment for the DTT edge plasma, comparing the state-of-the-art edge plasma codes SOLPS-ITER, SOLEDGE2D and UEDGE, but at nominal power and with neon as an extrinsic impurity. Although a quantitative change is expected for different impurity species, the conclusions drawn here would still apply. Currents and drifts are disabled to avoid further complications.

In contrast to [18] where observed differences between code predictions were in many instances mild, significantly greater discrepancies are observed for this higher-power impurity-seeded scenario.

In addition to a common OMP separatrix electron density of $6 \cdot 10^{19}\,\mathrm{m}^{-3}$ accurately reached by the codes, a targeted total radiated power of 20 MW is instead achieved with varying degree of success, by freely tuning the neon puffing. Significantly different injection rates of $4 \cdot 10^{19}$ Ne s^{-1}, $1 \cdot 10^{20}$ Ne s^{-1} and $6 \cdot 10^{19}$ Ne s^{-1} result in SOLPS-ITER, SOLEDGE2D and UEDGE.

The electron density and temperature at the OMP are very closely matched between SOLPS-ITER and SOLEDGE2D, as well as electron pressures among all three codes. But major discrepancies exist in main ion density (38%–138%), unified ion temperature (34%–112%) and Z_{eff} (33%–144%) at OMP, but also throughout much of the domain, in all the codes.

At the divertor targets, in the attached far-SOL, features related to the electron density/temperature profiles are inherited from the upstream, as in [18]. But, compared to [18], new discrepancies arise elsewhere, quantitatively in heat fluxes at the outer target (88%–178%) and qualitatively at the inner (single- vs. double-peak profiles), in the degree of detachment and in the location of reattachment onset.

In investigating possible underlying causes of the disagreement, inherent differences in the code equations are noted:

- *Extra terms.* Regions where SOLPS-ITER extra terms in the plasma equations attain some relative importance are identified, as in [18]. This notably occurs for the x-directed anomalous transport terms in the detached plasma regions.
- *Collision times and momentum sources.* Within the ITA here adopted, the difference in the collision times and friction

force of SOLPS-ITER and SOLEDGE2D, a function of the species mass and concentration, is always significant. The assessment of the corresponding changes in the solution is however non-trivial, even more so for the other momentum sources, also differing among the two codes. This finding hence urges on the adoption of the full Zhdanov closure in all the codes, as accomplished in [33, 43], which would also avoid the potential shortcomings of the simplified force-balance momentum equations for impurities utilised in UEDGE in this study.

None of the discrepancies observed in the outcomes can however be entirely traced back to any of the above, but still worthwhile investigating.

Conversely, understood instances and lessons learnt from our studies can be summarised as follows:

- *Over-penetration of neutrals.* The over-penetration of the puffed neutral deuterium in UEDGE, previously discovered in [18] and following from $T_D = T_i$, re-appears in this scenario, with a significantly enhanced effect at these higher power levels. UEDGE electron density is over-estimated by 38%–114% in the OMP core, and under-estimated in the SOL. The additional radial particle flux this extra penetration creates in the core results, for a fixed input power, in a redistribution of radial power flux between conductive and convective channels, driving differences in the electron and ion temperature profiles in UEDGE. The electron pressure is verified to still be in close agreement to that of SOLPS-ITER and SOLEDGE2D.
  The over-penetration also leads to a deuterium-dominated core plasma, hence correspondingly lowering Z_{eff} in UEDGE—the source of high ionisation stages being suppressed in the hot core plasma.
  Although [18] showed how this can be locally ameliorated by ad hoc neutral flux limiters, such a solution is scenario-specific and not appropriate for the entire plasma. Advanced neutral models in the like of [31] potentially offer a solution to these issues—but these must be demonstrated to agree well with kinetic neutral models in both the divertor regions and the upstream main chamber plasmas simultaneously, in order to have confidence.
- *Density flooring.* The artificial particle source supporting the minimum impurity ion densities ('density floor', similarly applied in all three codes) is found to spuriously generate an appreciable impurity particle imbalance, in fact creating high-charge species in low-temperature regions, and low-charge species in high-temperature regions. Though the imbalance is $\sim$1% in UEDGE, the density floor is a factor 10^3 higher in SOLEDGE2D, meaning the extra particle source is likely more significant.
  Unresolved disagreement is also the distribution of the radiation emission, in SOLEDGE2D resulting in a significantly higher radiation in the core and main-chamber SOL regions. The effect of the artificial density floor of low/medium neon charge states in the core is potentially a noteworthy factor—a concern for application to study power exhaust handling for divertor designs.
  These effects are anticipated to be worse for higher-Z impurities (e.g. argon, tungsten), given the greater number of charge states the minimum density floor is required to support. Care should be taken in impurity modelling in all three codes to ensure the density floor is set low enough to prevent this particle imbalance and its consequences, while avoiding numerical instabilities.
- *Activity around the secondary X-point.* In SOLEDGE2D, high ionisation stages existing in the cold edge plasma regions unaffected by the density floor remain unexplained. This is thus ascribed to the absence of an inward-pointing pinch for high neon ionisation stages, in conjunction with SOLEDGE2D extended mesh and lower friction forces in action—physically dubious as a whole, but potentially falling under the umbrella of non-negligible activity around the secondary X-point of a single null topology. With the sputtering of the main chamber wall being increasingly emphasised in the community [60, 61], and the dominant contributors being impurities, the importance of proper assessments of Z_{eff} in the far SOL grows, and hence does the quantification of impurity cross-field transport.
- *Atomic-molecular reactions.* In SOLPS-ITER, discarding neutral-neutral collisions and reducing the set of atomic-molecular reactions to SOLEDGE2D's is found to be even more impactful than in [18], and allows SOLPS-ITER to reach similar $P_{rad} \sim 20\,\mathrm{MW}$ and $1 \cdot 10^{20}\,\mathrm{Ne} \cdot \mathrm{s}^{-1}$ puffing rate as in SOLEDGE2D. In turn, this drastically reduces the disparity among the two codes—not entirely erasing all the observed differences nonetheless, nor being satisfactory overall, being able to reach such conditions in SOLPS-ITER only by simplifying the physical models.
- *Intricacies of an extended plasma mesh.* In opposition to the radiation-driven doubly-peaking heat flux profile at the inner target in UEDGE, the same feature in SOLEDGE2D is an artefact of the mesh construction. It results from the penalisation technique applied to the non-conformal cells misaligned to the wall in the far SOL, included by SOLEDGE2D's extended mesh. Guaranteeing ubiquitous cell conformity can be accomplished, e.g. at the expense of an enhanced complexity in the cell structure [62, 63].
  Also, ensuring an appropriate density floor would be particularly relevant for high-charge-state flooring in the cold plasma accounted for by an extended mesh, where the local plasma conditions could even threaten the applicability of the plasma equations in the first place.
  Last, low-density and/or low-temperature regions can violate the validity of both the reaction rates [18, 55] and the unified ion temperature equation. This is relevant for deeply-detached scenarios in the like of [64]'s, and in the far SOL of any scenario, respectively.
  The present study therefore clarifies how the benefits of extended plasma meshes (e.g. avoiding the artefacts related to the finite radial extent of the SOLPS-ITER plasma mesh, here again observed) come with in-kind challenges, in addition to those reported by [55], to be determined and resolved.

Understanding the different models and approximations used in edge plasma codes is paramount for the interpretation of

their predictions, and to understand their limitations—yet to be fully characterised and, crucially, to be compared with experimental data, as per our separate publication focused on Alcator C-Mod [19].

The outcomes of this work and of [18] can be used both in re-assessment of past work utilising these codes, as well as for informing the use and development of edge codes in the future. Immediate examples, meritorious of further investigations, are the SOLPS-ITER full-vessel mode under development [62, 63] (caveated by, at least, the known challenges above), emphasising and correcting for disparities resulting from advanced fluid vs. kinetic neutral models [31, 37, 65], and comparing the additional physical models (e.g. Zhdanov closure, separate ion energy equations in SOLEDGE2D, full impurity momentum equations in UEDGE), with currents and drifts [66, 67].

Acknowledgments

This work was made possible with fellowship support from Eni S.p.A. through the MIT Energy Initiative and is funded by Eni S.p.A., Contract N. 4310537045, in the framework of a 4-Ways Agreement between Eni, MIT, CFS and ENEA. Eni S.p.A. also supported the modelling activity at Politecnico di Torino related to this work through Contract N. 4310537045.

Acknowledgment to the help of the SOLPS-ITER, SOLEDGE2D and UEDGE teams is duely given, especially to X. Bonnin for the feedbacks regarding SOLPS-ITER, and to M. Umansky and T. Rognlien for the support in the UEDGE work.

Thanks is given also to M. Kryjak, G. Rubino and A. Sladkomedova, for the useful discussions while developing this work, and to V. Ostuni and R. Chamay for the ever-precious help.

ORCID iDs

M. Moscheni https://orcid.org/0000-0002-6355-7274
M. Wigram https://orcid.org/0000-0002-5376-128X
H. Wu https://orcid.org/0000-0002-2473-1532
C. Meineri https://orcid.org/0000-0001-5107-0357
C. Carati https://orcid.org/0000-0003-4001-9067
M. Greenwald https://orcid.org/0000-0002-4438-729X
P. Innocente https://orcid.org/0000-0001-8726-994X
B. LaBombard https://orcid.org/0000-0002-7841-9261
F. Subba https://orcid.org/0000-0002-8170-4792
R. Zanino https://orcid.org/0000-0003-0334-8275

References

[1] Eich T. *et al* 2013 Scaling of the tokamak near the scrape-off layer H-mode power width and implications for ITER *Nucl. Fusion* **53** 093031
[2] Zhang X. *et al* 2024 Experimental observations of bifurcated power decay lengths in the near Scrape-Off Layer of ST40 High Field Spherical Tokamak *Nucl. Mater. Energy* **41** 101772
[3] Pitts R. *et al* 2019 Physics basis for the first ITER tungsten divertor *Nucl. Mater. Energy* **20** 100696
[4] Pitts R. *et al* 2017 Physics conclusions in support of ITER W divertor monoblock shaping *Nucl. Mater. Energy* **12** 60–74
[5] Federici G. *et al* 2018 DEMO design activity in Europe: progress and updates *Fusion Eng. Des.* **136** 729–41
[6] Sorbom B. *et al* 2015 ARC: a compact, high-field, fusion nuclear science facility and demonstration power plant with demountable magnets *Fusion Eng. Des.* **100** 378–405
[7] LaBombard B. *et al* 2013 X-point target divertor concept and the Alcator DX high power divertor test facility *APS Division of Plasma Physics Meeting Abstracts* (*APS Meeting Abstracts* vol 2013) p CO4.002
[8] Kotschenreuther M., Valanju P.M., Mahajan S.M. and Wiley J.C. 2007 On heat loading, novel divertors and fusion reactors *Phys. Plasmas* **14** 072502
[9] Ryutov D.D. and Soukhanovskii V.A. 2015 The snowflake divertor *Phys. Plasmas* **22** 110901
[10] Nallo G., Mazzitelli G., Savoldi L., Subba F. and Zanino R. 2019 Self-consistent modelling of a liquid metal box-type divertor with application to the divertor tokamak test facility: Li versus Sn *Nucl. Fusion* **59** 066020
[11] Kessel C. *et al* 2019 Critical exploration of liquid metal plasma-facing components in a fusion nuclear science facility *Fusion Sci. Technol.* **75** 886–917
[12] Martone R., Albanese R., Crisanti F., Pizzuto A. and Martin P. (eds) 2019 (available at: www.dtt-dms.enea.it/share/s/avvglhVQT2aSkSgV9vuEtw)
[13] Innocente P. *et al* 2017 *Exploration of DTT conventional and advanced divertor configurations by means of edge simulation codes* INIS-XA–21M3794 International Atomic Energy Agency (IAEA)
[14] Balbinot L., Rubino G., Casiraghi I., Meineri C., Frassinetti L., Aucone L., Mantica P., Innocente P. and Wigram M. 2023 Multi-code estimation of DTT edge transport parameters *Nucl. Mater. Energy* **34** 101350
[15] Bonnin X., Dekeyser W., Pitts R., Coster D., Voskoboynikov S. and Wiesen S. 2016 Presentation of the new SOLPS-ITER Code package for tokamak plasma edge modelling *Plasma Fusion Res.* **11** 1403102
[16] Bufferand H. *et al* 2017 Implementation of drift velocities and currents in SOLEDGE2D-EIRENE *Nucl. Mater. Energy* **12** 852–7
[17] Rognlien T., Milovich J., Rensink M. and Porter G. 1992 A fully implicit, time dependent 2-D fluid code for modeling tokamak edge plasmas *J. Nucl. Mater.* **196–198** 347–51
[18] Moscheni M. *et al* 2022 Cross-code comparison of the edge codes SOLPS-ITER, SOLEDGE2D and UEDGE in modelling a low-power scenario in the DTT *Nucl. Fusion* **62** 056009
[19] Wigram M. *et al* 2021 Application of edge codes to the new high-field tokamaks *63rd Annual Meeting of the APS Division of Plasma Physics* (*8–12 November 2021*)
[20] Rognlien T.D., Ryutov D.D., Mattor N. and Porter G.D. 1999 Two-dimensional electric fields and drifts near the magnetic separatrix in divertor tokamaks *Phys. Plasmas* **6** 1851–7
[21] Ballinger S. *et al* 2021 Simulation of the SPARC plasma boundary with the UEDGE code *Nucl. Fusion* **61** 086014
[22] Summers H.P., O'Mullane M.G., Whiteford A.D., Badnell N.R. and Loch S.D. 2007 ADAS: Atomic data, modelling and analysis for fusion *AIP Conf. Proc.* **901** 239–48
[23] Dux R. 2006 STRAHL user manual *Max-Planck-Institut für Plasmaphysik* (available at: www.semanticscholar.org/paper/STRAHL-User-Manual-Dux/c515b9ae3ad7403d288bbcc09a9a595513fbaa84)

[24] Behringer K. 1987 *Description of the impurity transport code 'STRAHL'* JET-R–87-08 Commission of the European Communities, Abingdon (UK). JET Joint Undertaking

[25] Angioni C. 2021 Impurity transport in tokamak plasmas, theory, modelling and comparison with experiments *Plasma Phys. Control. Fusion* **63** 073001

[26] Keilhacker M., Simonini R., Taroni A. and Watkins M. 1991 A scrape-off layer model for the study of impurity retention in the pumped divertor planned for JET *Nucl. Fusion* **31** 535

[27] Stangeby P. 2000 *The Plasma Boundary of Magnetic Fusion Devices* (*Series in Plasma Physics and Fluid Dynamics*) (Taylor & Francis) (https://doi.org/10.1088/0741-3335/43/2/702)

[28] Sytova E. *et al* 2020 Derivation of the friction and thermal force for SOLPS-ITER multicomponent plasma modeling *Phys. Plasmas* **27** 082507

[29] Smith G., Brown P.N., Campbell R.B., Knoll D.A., McHugh P.R., Rensink M.E. and Rognlien T.D. 1995 Techniques and results of tokamak-edge simulation *J. Nucl. Mater.* **220–222** 1024–7

[30] Braginskii S.I. 1965 *Transport Processes in a Plasma* vol 1 (Consultants Bureau) pp 205–311 (available at: https://api.semanticscholar.org/CorpusID:118480963)

[31] Uytven W.V., Dekeyser W., Blommaert M., Carli S. and Baelmans M. 2022 Assessment of advanced fluid neutral models for the neutral atoms in the plasma edge and application in ITER geometry *Nucl. Fusion* **62** 086023

[32] Dekeyser W. *et al* 2011 *B2-B2.5 code benchmarking* JUEL–4337

[33] Bufferand H. *et al* 2022 Implementation of multi-component Zhdanov closure in SOLEDGE3X *Plasma Phys. Control. Fusion* **64** 055001

[34] Borodin D.V., Schluck F., Wiesen S., Harting D., Börner P. *et al* 2022 Fluid, kinetic and hybrid approaches for neutral and trace ion edge transport modelling in fusion devices *Nucl. Fusion* **62** 086051

[35] Dudson B., Kryjak M., Muhammed H., Hill P. and Omotani J. 2023 Hermes-3: Multi-component plasma simulations with BOUT++ (https://doi.org/10.48550/arXiv.2303.12131)

[36] Bhatnagar P.L., Gross E.P. and Krook M. 1954 A model for collision processes in gases. I. Small amplitude processes in charged and neutral one-component systems *Phys. Rev.* **94** 511–25

[37] Kryjak M. *et al* 2023 Comparison of the new BOUT++ fluid edge code Hermes-3 to SOLEDGE2D-EIRENE in an example ST40 predictive scenario *65th Annual Meeting of the APS Division of Plasma Physics* (*30 October–3 November 2023*)

[38] Albanese R., Ambrosino R. and Mattei M. 2015 CREATE-NL+: a robust control-oriented free boundary dynamic plasma equilibrium solver *Fusion Eng. Des.* **96–97** 664–7

[39] Tonello E. 2024 Global modelling of helium Plasma-Wall Interaction experiments in ASDEX-Upgrade *PSI26 Conf.* pp 4–092

[40] Subba F., Coster D., Moscheni M. and Siccinio M. 2021 SOLPS-ITER modeling of divertor scenarios for EU-DEMO *Nucl. Fusion* **61** 106013

[41] Itskov M. 2009 *Tensor Algebra and Tensor Analysis for Engineers: With Applications to Continuum Mechanics* 2nd edn (Springer)(https://doi.org/10.1007/978-3-540-93907-8)

[42] Zhdanov V. 2002 *Transport Processes in Multicomponent Plasma* (Taylor and Francis)(https://doi.org/10.1201/9781482265101)

[43] Makarov S.O., Coster D.P., Rozhansky V.A., Stepanenko A.A., Zhdanov V.M., Kaveeva E.G., Senichenkov I.Y. and Bonnin X. 2021 Equations and improved coefficients for parallel transport in multicomponent collisional plasmas: Method and application for tokamak modeling *Phys. Plasmas* **28** 062308

[44] Rozhansky V. 2023 private communication

[45] Krasheninnikov S.I. and Kukushkin A.S. 2017 Physics of ultimate detachment of a tokamak divertor plasma *J. Plasma Phys.* **83** 155830501

[46] Zholobenko W., Stegmeir A., Griener M., Conway G.D., Body T., Coster D. and Jenko F. 2021 The role of neutral gas in validated global edge turbulence simulations *Nucl. Fusion* **61** 116015

[47] Quadri V. 2024 Edge plasma turbulence simulations in high density regimes *PSI26 Conf.* pp 3–046

[48] Rozhansky V., Kaveeva E., Baranovsky I. and Pitts R. 2022 Transport in the tokamak - reactor edge plasma with strong collisionality *Nucl. Mater. Energy* **33** 101316

[49] Wiesen S. *et al* 2018 On the role of finite grid extent in SOLPS-ITER edge plasma simulations for JET H-mode discharges with metallic wall *Nucl. Mater. Energy* **17** 174–81

[50] Moscheni M., Carr M., Dulla S., Maviglia F., Meakins A., Nallo G.F., Subba F. and Zanino R. 2021 Parametric study of the radiative load distribution on the EU-DEMO first wall due to SPI-mitigated disruptions *Fusion Eng. Des.* **172** 112917

[51] Moscheni M., Carr M., Dulla S., Maviglia F., Meakins A., Nallo G.F., Subba F. and Zanino R. 2020 Radiative heat load distribution on the EU-DEMO first wall due to mitigated disruptions *Nucl. Mater. Energy* **25** 100824

[52] Wang H.Q., Watkins J.G., Guo H.Y., Groth M., Jarvinen A.E., Leonard A.W., Ren J., Thomas D.M. and Boedo J. 2021 Effects of divertor electrical drifts on particle distribution and detachment near the divertor target plate in DIII-D *Phys. Plasmas* **28** 052509

[53] Ahn J.-W., Maingi R., Canik J.M., McLean A.G., Lore J.D., Park J.-K., Soukhanovskii V.A., Gray T.K. and Roquemore A.L. 2011 Effect of nonaxisymmetric magnetic perturbations on divertor heat and particle flux profiles in National Spherical Torus Experiment *Phys. Plasmas* **18** 056108

[54] Lee H. *et al* 2017 Thermographic studies of outer target heat fluxes on KSTAR *Nucl. Mater. Energy* **12** 541–7

[55] Rivals N., Tamain P., Marandet Y., Bonnin X., Bufferand H., Pitts R.A., Falchetto G., Yang H. and Ciraolo G. 2022 *Contrib. Plasma Phys.* **62** e202100182

[56] Kallenbach A. *et al* 2015 Partial detachment of high power discharges in ASDEX Upgrade *Nucl. Fusion* **55** 053026

[57] Stotler D., Battaglia D.J., Hager R., Kim K., Koskela T., Park G. and Reinke M.L. 2017 Kinetic neoclassical calculations of impurity radiation profiles *Nucl. Mater. Energy* **12** 1130–5

[58] Pitts R. *et al* 2011 Physics basis and design of the ITER plasma-facing components *J. Nucl. Mater.* **415** S957–64

[59] Lore J., Bonnin X., Park J.-S., Pitts R. and Stangeby P. 2022 High gas throughput SOLPS-ITER simulations extending the ITER database to strong detachment *Nucl. Fusion* **62** 106017

[60] Pitts R. 2024 Plasma-wall interaction impact of the ITER re-baseline *PSI26 Conf.* pp 1–117

[61] Schmid K. 2024 Full W ITER: assessment of expected W erosion and implications of boronization on fuel retention *PSI26 Conf.* pp 1–123

[62] Dekeyser W. *et al* 2021 Plasma edge simulations including realistic wall geometry with SOLPS-ITER *Nucl. Mater. Energy* **27** 100999

[63] Dekeyser W. 2024 Simulations of the ITER scrape-off layer plasma up to the first wall with SOLPS-ITER *PSI26 Conf.* pp 2–085

[64] Verhaegh K. *et al* 2022 Spectroscopic investigations of detachment on the MAST Upgrade Super-X divertor *Nucl. Fusion* **63** 016014
[65] Coster D.P., Bonnin X., Braams B., Reiter D. and Schneider R. 2004 Simulation of the edge plasma in tokamaks *Phys. Scr.* **2004** 7
[66] Rubino G. 2024 Benchmarking SOLPS-ITER and SONIC edge transport codes in JT-60SA tokamak plasma conditions *PSI26 Conf.* pp 3–78
[67] Bonnin X. 2024 Comparing various plasma edge codes for predictions of ITER divertor operation and SOLPS-ITER wide grids recent developments *PSI26 Conf.* pp 2–073